



# Rapid Growth of Seed Black Holes during Early Bulge Formation

Kohei Inayoshi<sup>1</sup>, Riouhei Nakatani<sup>2</sup>, Daisuke Toyouchi<sup>3</sup>, Takashi Hosokawa<sup>4</sup>, Rolf Kuiper<sup>5</sup>, and Masafusa Onoue<sup>1,6,7</sup>

<sup>1</sup>Kavli Institute for Astronomy and Astrophysics, Peking University, Beijing 100871, People's Republic of China; [inayoshi@pku.edu.cn](mailto:inayoshi@pku.edu.cn)

<sup>2</sup>RIKEN Cluster for Pioneering Research, 2-1 Hirosawa, Wako-shi, Saitama 351-0198, Japan

<sup>3</sup>Research Center for the Early Universe (RESCEU), The University of Tokyo Hongo, 7-3-1, Bunkyo-ku Tokyo, 113-0033, Japan

<sup>4</sup>Department of Physics, Kyoto University, Kyoto 606-8502, Japan

<sup>5</sup>Zentrum für Astronomie der Universität Heidelberg, Institut für Theoretische Astrophysik, Albert-Ueberle-Straße 2, D-69120 Heidelberg, Germany

<sup>6</sup>Kavli Institute for the Physics and Mathematics of the Universe (Kavli IPMU, WPI), The University of Tokyo, Chiba 277-8583, Japan

<sup>7</sup>Max-Planck-Institut für Astronomie, Königstuhl 17, D-69117 Heidelberg, Germany

Received 2021 October 21; revised 2021 December 26; accepted 2021 December 29; published 2022 March 21

## Abstract

We study the early growth of massive seed black holes (BHs) via accretion in protogalactic nuclei where the stellar bulge component is assembled, performing axisymmetric two-dimensional radiation hydrodynamical simulations. We find that when a seed BH with  $M_{\bullet} \sim 10^5 M_{\odot}$  is embedded in dense metal-poor gas ( $Z = 0.01 Z_{\odot}$ ) with a density of  $\gtrsim 100 \text{ cm}^{-3}$  and bulge stars with a total mass of  $M_{\star} \gtrsim 100 M_{\star}$ , a massive gaseous disk feeds the BH efficiently at rates of  $\gtrsim 0.3\text{--}1 M_{\odot} \text{ yr}^{-1}$ , and the BH mass increases nearly tenfold within  $\sim 2 \text{ Myr}$ . This rapid accretion phase lasts until a good fraction of the gas bounded within the bulge accretes onto the BH, although the feeding rate is regulated owing to strong outflows driven by ionizing radiation emitted from the accreting BH. The transient growing mode can be triggered for seed BHs formed in massive dark-matter halos with masses of  $\gtrsim 10^9 M_{\odot}$  at  $z \sim 15\text{--}20$  (the virial temperature is  $T_{\text{vir}} \simeq 10^5 \text{ K}$ ). The host halos are heavier and rarer than those of typical first galaxies, but are more likely to end up in quasar hosts by  $z \simeq 6$ . This mechanism naturally yields a mass ratio of  $M_{\bullet}/M_{\star} > 0.01$  higher than the value seen in the local universe. The existence of such overmassive BHs provides us with a unique opportunity to detect highly accreting seed BHs at  $z \sim 15$  with AB magnitude of  $m_{\text{AB}} \sim 26\text{--}29 \text{ mag}$  at  $2 \mu\text{m}$  (rest frame  $10 \text{ eV}$ ) by the upcoming observations by the James Webb Space Telescope and Nancy Grace Roman Space Telescope.

*Unified Astronomy Thesaurus concepts:* Supermassive black holes (1663); Quasars (1319); High-redshift galaxies (734)

## 1. Introduction

Supermassive black holes (SMBHs) are one of the most essential objects that comprise galaxies, and their coevolution with host galaxies are suggested by the empirical relations between BH masses and galaxy properties seen in the local universe (e.g., Magorrian et al. 1998; Ferrarese & Merritt 2000; Kormendy & Ho 2013). Nevertheless, the origin of those SMBHs remains one of the most intriguing and longest-standing unsolved puzzles in astrophysics. In the past few decades, the discoveries of very luminous quasars in the high-redshift universe ( $z > 6$ ) have revealed that SMBHs with masses greater than  $\sim 10^9 M_{\odot}$  formed within the first billion years after the Big Bang (e.g., Fan 2006; Willott et al. 2010; Mortlock et al. 2011; Wu et al. 2015; Bañados et al. 2018; Wang et al. 2021; Yang et al. 2021). Beyond the rarest and most massive SMBHs that represent the tip of the iceberg of the high-redshift BH population, a recent wide-field survey with Subaru Hyper Suprime-Cam (HSC) brings the total number of  $z > 6$  quasars to nearly 200 and enables us to construct their luminosity function down to the faint-end regime (Matsuoka et al. 2016, 2018). The BH mass and host galaxy's properties of those low-luminosity quasars at  $z > 6$  have also been extensively investigated in order to construct the BH mass distribution at  $z > 6$  and understand the early coevolution between BHs and galaxies (e.g., Onoue et al. 2019; Izumi et al. 2019).

The existence of those high-redshift quasars requires their quick assembly mechanisms (Volonteri 2012; Haiman 2013; Inayoshi et al. 2020), for instance, rapid gas collapse into the nuclei of early protogalaxies (Volonteri & Rees 2005; Inayoshi et al. 2016; Toyouchi et al. 2021) and the formation of massive heavy seed BHs through primordial star formation (Omukai 2001; Bromm & Loeb 2003; Lodato & Natarajan 2006; Shang et al. 2010; Latif et al. 2013; Regan et al. 2014; Inayoshi et al. 2014; Becerra et al. 2015; Chon et al. 2018; Wise et al. 2019; Regan et al. 2020; Sassano et al. 2021) and runaway stellar mergers in dense regions (Devecchi & Volonteri 2009; Sakurai et al. 2017; Tagawa et al. 2020; Chon & Omukai 2020). In most previous studies, those efficient BH assembly processes are considered to take place in atomically cooling dark-matter (DM) halos with virial temperatures of  $T_{\text{vir}} \gtrsim 10^4 \text{ K}$ , (corresponding to DM halo masses of  $M_{\text{h}} \gtrsim 10^7 M_{\odot}$  at  $z \sim 10\text{--}15$ ), where typical first galaxies would form (Bromm & Yoshida 2011). However, a majority of cosmological simulations have suggested that the subsequent growth of seed BHs formed in typical first galaxies with shallow gravitational potential would be strongly quenched by various feedback processes including supernova (SN) explosions of forming massive stars and radiative/mechanical outputs associated with BH accretion (e.g., Dubois et al. 2013; Prieto & Escala 2016; Anglés-Alcázar et al. 2017; Habouzit et al. 2017; Latif et al. 2018).

Recently, semi-analytical studies by Lupi et al. (2021) and Li et al. (2021b) have proposed that BH seeding processes preferentially occur in highly biased, overdense regions of the universe where quasars form by  $z \simeq 6$ . The quasar progenitor halos are substantially heavier than those hosting first galaxies,



Original content from this work may be used under the terms of the [Creative Commons Attribution 4.0 licence](https://creativecommons.org/licenses/by/4.0/). Any further distribution of this work must maintain attribution to the author(s) and the title of the work, journal citation and DOI.

and their average mass exceeds  $M_h \sim 10^9 M_\odot$  by  $z \sim 20$  via quick assembly after the birth of BH seeds with  $M_* \sim 10^{4-5} M_\odot$ . Large-scale cosmological simulations demonstrate that cold gas streams feed the centers of such massive halos and sustain high-mass accretion rates until the mass of the galaxy reaches  $\sim 10^{12} M_\odot$  (Li et al. 2007; Sijacki et al. 2009; Di Matteo et al. 2012; Zhu et al. 2020; see also Dekel & Birnboim 2006). However, it is worth emphasizing that due to numerical limitations, cosmological simulations with a spatial resolution of  $\sim O(\text{kpc})$  treat feedback effects with sub-grid models. Therefore, it is essential to directly resolve physical processes in the nuclear region and investigate the growth phases of seed BHs hosted in massive halos that will end up as high-redshift quasars.

The nature of mass accretion onto BHs in galactic nuclei has been explored by analytical and numerical work. In the recent decade, radiation hydrodynamical (RHD) simulations have shown that rapid accreting flows can feed the BH at super-Eddington rates as long as a sufficient amount of gas already exists or is efficiently supplied to the vicinity of the BH horizon scale of  $r_{\text{nuc}} \simeq 10^{2-3} r_{\text{Sch}}$  (Ohsuga et al. 2005; Jiang et al. 2014; McKinney et al. 2015; Sądowski et al. 2015), where  $r_{\text{Sch}} \equiv 2GM_*/c^2$  is the Schwarzschild radius of the BH, where  $G$  is the gravitational constant, and  $c$  is the speed of light. Note that the nuclear size for a seed BH is as small as  $r_{\text{nuc}} \simeq 10^{-5} \text{ pc}$  ( $M_*/10^5 M_\odot$ ). However, ionizing radiation emitted from the accreting BH heats the gas inflowing from the BH gravitational influence radius of  $\sim 1\text{--}10 \text{ pc}$ , within which the BH gravitational energy dominates the gas thermal energy. Thus, the mass accretion rate is generally self-regulated below the Eddington value (Ciotti & Ostriker 2001; Milosavljević et al. 2009; Johnson et al. 2011; Park & Ricotti 2011, 2012; Jeon et al. 2012; Park et al. 2017; Smith et al. 2017).

Accordingly, RHD simulations that cover the BH influence radii and resolve sub-parsec scales showed that when the BH is embedded in a dense gas cloud so that the gas inflowing rate from the BH influence radius substantially exceeds the Eddington value, the global quasi-steady structure of rapid inflows is maintained (Inayoshi et al. 2016). In this case, since the emergent radiation flux is reduced by photon trapping and dust absorption in the flow, the gas inflow is not prevented by radiative feedback but leads to collapse of the ionized region surrounding the BH (see also Park et al. 2014; Sakurai et al. 2016; Yajima et al. 2017; Park et al. 2020). Moreover, anisotropic radiation produced from the accreting BH toward the polar regions moderates the negative feedback effect (Sugimura et al. 2017; Takeo et al. 2018), and mechanical feedback associated with strong outflows completely evacuates the polar regions but does not affect the gas dynamics of disk accretion (Takeo et al. 2020). Recent three-dimensional RHD simulations have shown that massive gas supply can be sustained when the dusty disk becomes sufficiently optically thick to ionizing radiation (Toyouchi et al. 2021). Applying the conditions to seed BHs in high-redshift protogalaxies, they found that BHs formed in massive DM halos with  $M_h \gtrsim 10^9 M_\odot$  in the early universe can experience a rapidly growing phase. We note that the halo conditions nicely agree with those suggested by previous studies in the context of seed formation (Lupi et al. 2021; Li et al. 2021b) and subsequent BH growth (e.g., Di Matteo et al. 2012).

However, those RHD simulation studies that focus on the intermediate physical scales within the gravitational influence radius of a seed BH ( $\lesssim 1\text{--}10 \text{ pc}$ ) have not taken into account the existence of its host galaxy, specifically stellar bulge

components. A previous study by Park et al. (2016) pioneered the role of stellar bulge gravity in promoting mass accretion onto seed BHs, using spherically symmetric one-dimensional RHD simulations that assume metal-free gas with a uniform initial distribution. They found that when the bulge mass is greater than a critical mass of  $\sim 10^6 M_\odot$ , the bulge gravity leads to gas accumulation and increases the BH fueling rate.

In this paper, we investigate the dynamics of accreting and outflowing gas in the intermediate missing region surrounding a massive seed BH in protogalaxies, performing a series of axisymmetric two-dimensional RHD simulations with a sufficiently large computation domain covering  $\sim 0.1\text{--}100 \text{ pc}$  that enables us to capture the multi-scale physics properly. We consider a massive metal-polluted cloud with metallicity of  $Z = 0.01 Z_\odot$  concentrated inside a massive DM halo, adopting initial conditions of gas motivated by cosmological simulations. We consider bulge stars formed in the protogalaxies that cause two relevant effects on BH feeding. First, since the bulge mass is considered to be heavier than the BH mass (for instance,  $M_*/M_\bullet \simeq 10^3$  in the local universe), a larger amount of gas can be accumulated from larger scales of  $\sim O(\text{kpc})$  due to additional stellar gravity and can efficiently be delivered into the BH gravitational sphere of influence. This would lead to rapid growth of BHs, as seen in the previous study. On the other hand, since the bulge consists of a number of stars (presumably young stars in protogalaxies), photoionization and heating caused by stellar radiation affect the thermal properties of the surrounding gas and would prevent the gas from feeding the BH. In our study, we quantify the critical conditions required for rapid growth of BHs induced by the galactic bulges.

One of the most interesting questions is how and when the BH-galaxy correlations were established. To answer this, we apply our RHD simulation results to seed formation in the cosmological framework of galaxy formation and translate the conditions required for rapid BH accretion in terms of the properties of the host protogalaxies and halos. We find that this BH-growth mechanism naturally yields a mass ratio of  $M_*/M_\bullet > 0.01$  at  $z \gtrsim 10$ , which is significantly higher than the canonical value seen in the local universe (Kormendy & Ho 2013) but is suggested from the observations of the brightest quasars at  $z > 6$  (Wang et al. 2010, 2013; Pensabene et al. 2020). Furthermore, the highly accreting seed BHs with  $M_\bullet \simeq 10^{5-6} M_\odot$  produce intense radiation with luminosities of  $\sim 10^{44-45} \text{ erg s}^{-1}$ . Therefore, the existence of such *overmassive* BHs provides us with a unique opportunity to detect seed BHs in the very early universe with upcoming deep near-infrared observations by, e.g., James Webb Space Telescope (JWST) and Nancy Grace Roman Space Telescope (RST). The result would shed the light on the unresolved coevolutionary process between BHs and galaxies in the early universe.

The rest of the paper is organized as follows. In Section 2, we first describe the numerical method and settings of our two-dimensional RHD simulations. In Section 3, we present the simulation results and their dependence on physical parameters that characterize the bulge and halo properties. Estimating the radiative luminosity from the highly accreting BHs, we quantify the detectability of the signature in upcoming observations by JWST and RST. In Section 4, based on the simulation results, we provide a theoretical explanation for the conditions required to promote rapid accretion onto BH seeds in protogalaxies. In Section 5, we discuss the conditions for rapid BH accretion in the framework of the hierarchical structure formation, the  $M_*/M_\bullet$  ratio expected in the early bulge formation stage, and implications for

the measurements of quasar lifetime. Finally, we summarize our findings in Section 6.

## 2. Method

### 2.1. Basic Equations

We solve the axisymmetric two-dimensional hydrodynamical equations using the open-source code `PLUTO` (Mignone et al. 2007), which has been modified to study massive star formation and the evolution of protoplanetary disks (e.g., Kuiper et al. 2010, 2011; Nakatani et al. 2018a, 2018b). A detailed description of the code and its applications to many other astrophysical systems are shown in Kuiper et al. (2020). In particular, we update the specific version of the code to investigate the physics of BH feeding and feedback in the high-redshift protogalactic nuclei.

The basic equations we solve are as follows: the equation of continuity,

$$\frac{\partial \rho}{\partial t} + \nabla \cdot (\rho \mathbf{v}) = 0, \quad (1)$$

and the equation of motion,

$$\frac{\partial(\rho v_r)}{\partial t} + \nabla \cdot (\rho v_r \mathbf{v}) = -\frac{\partial p}{\partial r} + \rho \frac{v_\theta^2 + v_\phi^2}{r} - \rho \frac{\partial \Phi}{\partial r} + (\nabla \cdot \boldsymbol{\sigma})_r + f_{\text{rad},r}, \quad (2)$$

$$\frac{\partial(\rho v_\theta)}{\partial t} + \nabla \cdot (\rho v_\theta \mathbf{v}) = -\frac{1}{r} \frac{\partial p}{\partial \theta} - \rho \frac{v_\theta v_\phi}{r} + \rho \frac{v_\phi^2}{r} \cot \theta + (\nabla \cdot \boldsymbol{\sigma})_\theta + f_{\text{rad},\theta}, \quad (3)$$

$$\frac{\partial(\rho v_\phi)}{\partial t} + \nabla^l \cdot (\rho v_\phi \mathbf{v}) = (\nabla \cdot \boldsymbol{\sigma})_\phi \quad (4)$$

where  $\rho$  is the mass density,  $\mathbf{v}$  is the velocity,  $p$  is the gas pressure,  $\Phi$  is the gravitational potential,  $\boldsymbol{\sigma}$  is the stress tensor due to viscosity, and  $f_{\text{rad},r}$  and  $f_{\text{rad},\theta}$  are the radial and polar components of the radiation force, respectively.

We solve the energy equation of

$$\frac{\partial E}{\partial t} + \nabla \cdot (H \mathbf{v}) = -\rho v_r \frac{\partial \Phi}{\partial r} + (\boldsymbol{\sigma} \cdot \nabla) \mathbf{v} + \Gamma - \Lambda, \quad (5)$$

where  $E = (1/2)\rho v^2 + \rho e$  and  $H = E + p$  are the total energy density and enthalpy per unit volume, and  $e$  is the internal energy per unit mass. The equation of state for ideal gas is assumed as

$$p = (\gamma - 1)\rho e, \quad (6)$$

where the adiabatic exponent  $\gamma$  depends on the chemical abundances and gas temperature (e.g., Omukai & Nishi 1998). The first and second terms on the right-hand side present work done by the gravitational force and viscous heating. The last two terms are volumetric radiative cooling and heating (in units of  $\text{erg s}^{-1} \text{cm}^{-3}$ ).

The gravitational potential is set to

$$\Phi = -\frac{GM_\bullet}{r} + \Phi_\star(r) + \Phi_{\text{DM}}(r), \quad (7)$$

where  $M_\bullet$  is the BH mass, and  $\Phi_\star$  and  $\Phi_{\text{DM}}$  are the gravitational potential owing to bulge stars and a DM halo, respectively. We here do not consider the self-gravity of gas. For the bulge

stellar potential, we assume that the stellar mass density profile follows a Hernquist profile, and thus the potential is given by

$$\Phi_\star(r) = -\frac{GM_\star}{r + r_c}, \quad (8)$$

(Hernquist 1990), where  $M_\star$  is the total bulge mass, and  $r_c$  is the core radius. Note that the bulge mass increases with time at a given star formation rate (SFR; see Section 2.5). With the stellar mass distribution, the velocity dispersion of stars at the half-mass-radius of  $R_e = (1 + \sqrt{2})r_c$  is analytically calculated as  $\sigma_e \simeq 0.23\sqrt{GM_\star/r_c}$  (see Appendix A).<sup>8</sup> Assuming that the bulge stellar component in high-redshift protogalaxies obeys the  $M_\star$ – $\sigma_e$  relation (Kormendy & Ho 2013), the core radius is set to

$$r_c \simeq 6.5 \text{ pc} \left( \frac{M_\star}{10^7 M_\odot} \right)^{0.47}. \quad (9)$$

Note that the observed slope of the  $R_e$ – $M_\star$  relation is known to depend on the stellar mass, galaxy type, and redshift (e.g., Shen et al. 2003; Mowla et al. 2019; Li et al. 2021a; Kawinwanichakij et al. 2021). For the DM potential, we consider a Navarro–Frenk–White (NFW) potential (Navarro et al. 1997; Mo et al. 1998), approximately written as

$$\Phi_{\text{DM}}(r) = -\frac{2k_B T_{\text{vir}}}{\mu m_p} \frac{\ln(1 + r/r_s)}{r/r_s} f(c_N), \quad (10)$$

where  $k_B$  is the Boltzmann constant,  $\mu$  is the mean molecular weight of gas,  $T_{\text{vir}}$  and  $r_{\text{vir}}$  are the virial temperature and virial radius of the halo, respectively,  $r_s$  ( $\equiv r_{\text{vir}}/c_N$ ) is the characteristic radius of the NFW density profile,  $c_N$  is the concentration factor, and  $f(c_N) = c_N/[\ln(1 + c_N) - c_N/(1 + c_N)]$ . We model the dependence of the mean concentration on halo mass  $M_h$  and redshift  $z$ :  $c_N \simeq 1.56 (M_h/10^9 M_\odot)^{-0.13} [(1 + z)/21]^{-1}$  (Bullock et al. 2001).

In our axisymmetric simulations without magnetohydrodynamical (MHD) effects, angular momentum transport in the accreting flow is given by imposing explicit viscosity. The viscous stress tensor is given by

$$\sigma_{ij} = \rho \tilde{\nu} \left[ \left( \frac{\partial v_j}{\partial x_i} + \frac{\partial v_i}{\partial x_j} \right) - \frac{2}{3} (\nabla \cdot \mathbf{v}) \delta_{ij} \right], \quad (11)$$

where  $\tilde{\nu}$  is the shear viscosity, and the bulk viscosity is neglected. To mimic angular momentum transport associated with MHD turbulence driven by the magnetorotational instability (MRI) in a sufficiently ionized disk (e.g., Balbus & Hawley 1998; Stone & Pringle 2001; McKinney & Gammie 2004; Bai 2011; Narayan et al. 2012), we assume the azimuthal components of the shear tensor are nonzero and, in spherical polar coordinates, are given by

$$\sigma_{r\phi} = \rho \tilde{\nu} \frac{\partial}{\partial r} \left( \frac{v_\phi}{r} \right), \quad (12)$$

<sup>8</sup> Park et al. (2016) calculated the bulge size so that the average stellar mass density within  $r_c$  is comparable to that of the Milky Way. Namely, they adopt  $r_c = 50 \text{ pc} (M_\star/10^7 M_\odot)^{1/3}$ , which yields  $M_\star \simeq 2.5 \times 10^{11} M_\odot (\sigma_e/200 \text{ km s}^{-1})^3$  and underestimates the velocity dispersion of bulge stars compared to that observed in the local universe.



$$\sigma_{\theta\phi} = \rho \tilde{\nu} \frac{\sin \theta}{r} \frac{\partial}{\partial \theta} \left( \frac{v_\phi}{\sin \theta} \right) \quad (13)$$

(e.g., Stone et al. 1999; Fernández & Metzger 2013; Inayoshi et al. 2019). The strength of anomalous shear viscosity is calculated with the  $\alpha$ -prescription (Shakura & Sunyaev 1973),

$$\tilde{\nu} = \alpha \frac{c_s^2}{\Omega_K} \cdot \exp\left(-\frac{|z|}{H}\right), \quad (14)$$

where  $\alpha$  is the viscous parameter,  $c_s$  is the sound speed,  $\Omega_K \equiv (GM_*/r^3)^{1/2}$ , and  $H(\equiv c_s/\Omega_K)$  is the disk scale height. Note that the exponential factor imposes that the viscous process is active near the mid-plane. The strength of viscosity is set to

$$\alpha = \alpha_0 + \alpha_{\max} \exp\left[-\left(\frac{\rho_{\text{crit}}}{\rho}\right)^2\right]. \quad (15)$$

The first term corresponds to the strength of MRI turbulence, and the value is set to  $\alpha_0 = 0.01$  (e.g., Zhu & Stone 2018; Takasao et al. 2018). The second term characterizes the torque caused by non-axisymmetric structure (e.g., spiral arms) excited in a marginally unstable disk against its self-gravity. The density threshold, above which viscosity turns on, is assumed to be  $\rho_{\text{crit}} \equiv \Omega_K^2/(\pi G) \simeq 2.2 \times 10^{-21} (M_*/10^5 M_\odot)(r/10 \text{ pc})^{-3} \text{ g cm}^{-3}$ . This choice is motivated by the following reasons. The local gravitational instability of a rotating disk is described by Toomre's  $Q$  parameter (Toomre 1964) defined by

$$Q \equiv \frac{c_s \kappa_\Omega}{\pi G \Sigma}, \quad (16)$$

where  $\kappa_\Omega^2 = 4\Omega^2 + d\Omega^2/d \ln r$  is the epicyclic frequency, and  $\Sigma$  is the disk surface density. For a geometrically thin cold disk around a point mass, the  $Q$ -value is approximated to  $Q \simeq \Omega_K^2/(2\pi G \rho) = 0.5(\rho_{\text{crit}}/\rho)$ . Thus, the second term of the right-hand side of Equation (15) is written as  $\propto \exp(-4Q^2)$ , which is a commonly used parameterization of the effective viscosity adopted in semi-analytical models of a self-gravitating disk;  $\propto \exp(-Q^A/B)$  where  $A > 0$  and  $B > 0$  (Zhu et al. 2009; Takahashi et al. 2013; see also Kratter & Lodato 2016). The value of  $\alpha_{\max}$  depends on the level of non-axisymmetric structures in a disk. A previous three-dimensional RHD simulation study of a dusty circumnuclear disk around a BH shows that the mass inflow velocity is as high as a substantial fraction of the freefall velocity due to strong torque caused by spiral arms in the disk, indicating  $\alpha_{\max} \simeq O(1)$  (Toyouchi et al. 2021). We here adopt  $\alpha_{\max} = 2$  (Hirano et al. 2014; Fukushima et al. 2020). The critical  $Q$ -value for the onset of gravitational torque caused by spiral arms in a disk is considered to be  $Q \sim 1$ , but the exact value depends on various properties of the disk (e.g., cooling, heating, and disk irradiation). We note that in our viscous model, the second term in Equation (15) becomes larger than  $\alpha_0$  when  $Q \leq 1.15$ .

We consider cooling processes associated with chemical reactions and radiative processes of metal-polluted gas, which is composed of 11 chemical species (H, H<sub>2</sub>, e<sup>-</sup>, H<sup>+</sup>, H<sub>2</sub><sup>+</sup>, H<sup>-</sup>, He, He<sup>+</sup>, He<sup>++</sup>, C<sup>+</sup>, and O) and dust grains. We solve the chemical reaction network of primordial gas among the nine species (hydrogen and helium) and adopt the same reaction rate

coefficients compiled in Li et al. (2021b). The cooling rates by collisional excitation and ionization, radiative recombination of H, He, He<sup>+</sup> atoms, their free-free emission (Glover & Jappsen 2007), and the fine-structure lines of C<sup>+</sup> and O (Hollenbach & McKee 1989) are calculated in the optically thin limit. The cooling rate of H<sub>2</sub> rovibrational transitions is included (Galli & Palla 1998), but this effect is negligible under strong H<sub>2</sub>-dissociating photons produced from bulge stars. We assume that the amount of heavy elements in gas-phase and dust grains is proportional to the relative metallicity  $Z/Z_\odot$  and give the dust-to-gas mass ratio by  $0.01 Z/Z_\odot$ .

We implement photoionization of H, He, and He<sup>+</sup> by intense BH radiation and associated photoheating by solving radiation transfer (RT). In addition, we consider H<sub>2</sub>-dissociating radiation in the Lyman–Werner (LW) band and the X-ray radiation background produced from bulge stars surrounding the accreting BH and its gravitational influence radius. As for X-ray irradiation, the secondary ionization effect caused by energetic primary electrons is considered (Inayoshi & Omukai 2011, references therein). More detailed treatments of BH and stellar radiation are described in Section 2.2.

## 2.2. Radiation Transfer

We quantify the radiative heating rate  $\Gamma$ , ionization rate  $\zeta$ , and radiation pressure force by solving the RT of both direct and diffusion components. We adopt a hybrid RT scheme (e.g., Kuiper et al. 2020): the direct component emitted from the central BH is solved by means of the multifrequency ray-tracing method, while the diffusive component owing to thermal (re-)emission by dust grains is solved by a flux-limited diffusion (FLD) approximation.

The direct component of the flux associated with BH accretion is the primary source of radiative feedback that affects the properties of accreting flows. The radiation flux can analytically be expressed as

$$F_\nu(r, \theta, t) = \frac{\mathcal{L}_{\nu}(\theta, t)}{4\pi r^2} e^{-(\tau_{g,\nu} + \tau_{d,\nu})}, \quad (17)$$

where  $\nu$  is a frequency of radiation,  $F_\nu(r, \theta, t)$  is the radial component of the specific radiative flux at a distance of  $r$  from the center toward a direction of  $\theta$  radian from the pole, and  $\mathcal{L}_{\nu}/(4\pi r^2)$  is the unattenuated specific radiative flux that includes the anisotropic degree (see Section 2.3). The optical depth of gas and dust to a photon at a frequency of  $\nu$  are calculated as

$$\tau_{g,\nu} = \int_{r_{\text{in}}}^r \sum_i n_i(\hat{r}, \theta, t) \cdot \sigma_{i,\nu} d\hat{r}, \quad (18)$$

$$\tau_{d,\nu} = \int_{r_{\text{in}}}^r \rho(\hat{r}, \theta, t) \cdot \kappa_{d,\nu} d\hat{r}, \quad (19)$$

respectively, where  $n_i$  is the number density of the  $i$ -th component ( $i = \text{H, He, and He}^+$ ),  $\sigma_{i,\nu}$  is the bound-free cross section (Verner et al. 1996; Yan et al. 1998), and  $\kappa_{d,\nu}$  is the dust opacity. In our simulations, we use the opacity table taken from Draine & Lee (1984) in the RT calculation for nonionizing radiation, while the attenuation level of ionizing (EUV) radiation is calculated by using one single opacity value of  $\kappa_{d,0} \simeq 2.8 [Z/(0.01 Z_\odot)] \text{ cm}^2 \text{ g}^{-1}$  (per gas mass). The radiation flux absorbed by each component is used for calculating the heating and ionization rates ( $\Gamma$  and  $\zeta$ ) owing to EUV irradiation

and the dust heating rate  $S_*$  caused by all of the photons emitted from the accreting BH. Those rates are estimated so that the number of photons emitted along any line of sight equals the number of photoionization in that direction over any time interval (e.g., Whalen & Norman 2006; Inayoshi et al. 2016; Nakatani et al. 2018a, 2018b). We note that the component of diffusive EUV radiation produced by radiative recombination of gas is not considered because UV feedback onto accretion flows is dominated by the direct component emitted from the central bright object (e.g., Hosokawa et al. 2011). However, in order to calculate the size of an ionized region precisely, we need to take into account that recombinations directly to the ground state lead to immediate ionization of a hydrogen atom in the vicinity. To treat this effect, we adopt the “on-the-spot” approximation using the case-B recombination rate coefficient.

The diffusion component of infrared (IR) thermal radiation produced by dust grains is treated with a gray-approximated FLD method by solving the moment equation

$$\frac{\partial E_{\text{rad}}}{\partial t} + \nabla \cdot \mathbf{F}_{\text{IR}} = \rho \kappa_{\text{P}} c (a_{\text{R}} T_{\text{d}}^4 - E_{\text{rad}}) + S_*, \quad (20)$$

where  $E_{\text{rad}}$  is the radiation energy density,  $T_{\text{d}}$  is the dust temperature,  $\kappa_{\text{P}}$  is the Planck-mean dust opacity,  $a_{\text{R}}$  is the radiation constant, and  $\mathbf{F}_{\text{IR}}$  is the IR radiation flux (re-)emitted from dust and is approximated as

$$\mathbf{F}_{\text{IR}} = -\frac{\lambda c}{\rho \kappa_{\text{R}}} \nabla E_{\text{rad}}, \quad (21)$$

where  $\kappa_{\text{R}}$  is the Rosseland-mean dust opacity, and  $\lambda$  is the flux limiter (Levermore & Pomraning 1981). We solve the RT equations with an implicit solver imposing a zero-gradient boundary condition for the radiation energy. The dust temperature is calculated separately from the radiation temperature by using the two-temperature linearization approach (see more details in Kuiper et al. 2020).

With the direct component of radiation incident from the BH, we calculate the outward radiation force through electron scattering, bound-free transitions, and attenuation by dust grains. The diffusive component exerts the IR radiation force to both the radial and polar directions.

### 2.3. BH Radiation Model

We inject photons from the unresolved central region (i.e., the sink cell) to the computational domain, supposing that a compact accretion disk forms around the nuclear BH. Following Sazonov et al. (2004), we consider a broadband radiation spectral energy distribution (SED) obtained from the averaged quasar samples

$$L_{*,\nu} = \begin{cases} L_0 \left( \frac{\nu}{\nu_0} \right)^{-0.6} & (\nu_{\text{min}} \leq \nu < \nu_0), \\ L_0 \left( \frac{\nu}{\nu_0} \right)^{-1.5} & (\nu_0 \leq \nu \leq \nu_{\text{max}}), \end{cases} \quad (22)$$

where  $h\nu_0 = 10$  eV,  $h\nu_{\text{min}} = 1$  eV, and  $h\nu_{\text{max}} = 1$  keV. With this spectral shape, the bolometric (frequency integrated) luminosity is calculated as  $L_* = \int_{\nu_{\text{min}}}^{\nu_{\text{max}}} L_{*,\nu} d\nu \simeq 3.3 \nu_0 L_0$ , and the total EUV luminosity ( $h\nu \geq h\nu_{\text{Ly}} \equiv 13.6$  eV) is  $L_{\text{EUV}} \simeq 1.5 \nu_0 L_0$ . The

normalization of the luminosity is determined as a function of the mass accretion rate onto the BH. We note that the spectral power-law indices we adopt are consistent with those obtained from the stacked UV (rest-frame wavelengths 600–2500 Å) spectrum of 53 luminous quasars at  $z \simeq 2.4$  with a correction for the intervening Lyman forest and Lyman continuum absorption (Lusso et al. 2015); namely, the continuum spectrum is approximated by a broken power law with indices of  $\simeq -0.61 \pm 0.01$  at  $\nu < \nu_0$  and  $\simeq -1.7 \pm 0.61$  at  $\nu \geq \nu_0$ , respectively.

We set a model for radiation luminosity emitted from the accreting BH as

$$\frac{L_*}{L_{\text{Edd}}} = \begin{cases} \dot{m} & (\dot{m} < 2), \\ 2 \left[ 1 + \ln \left( \frac{\dot{m}}{2} \right) \right] & (\dot{m} \geq 2), \end{cases} \quad (23)$$

where  $L_{\text{Edd}}$  is the Eddington luminosity,  $\dot{m}$  is the BH mass accretion rate normalized by the Eddington rate  $\dot{M}_{\text{Edd}} [\equiv L_{\text{Edd}}/(\eta_0 c^2)]$ , and  $\eta_0 = 0.1$  is the radiative efficiency in the sub-Eddington and mildly Eddington regime (Shakura & Sunyaev 1973). The radiative luminosity at  $\dot{m} > 2$  is obtained from Watarai et al. (2000) in a slim-disk model (Abramowicz et al. 1988). We note that the two expressions in Equation (23) are broadly consistent with the results obtained with general relativistic, (magneto-)RHD simulations (Jiang et al. 2014; Sądowski et al. 2015; see also a model comparison in Inayoshi et al. 2020).

Furthermore, we assume isotropic/anisotropic radiation fields depending on the bolometric luminosity emitted from the accreting BH. When the radiative luminosity is lower than a critical value of  $L_{\text{crit}}$ , we inject the isotropic radiation flux from the center. On the other hand, when the BH is rapidly growing and  $L_* > L_{\text{crit}}$ , the radiation flux with  $L_{\text{crit}}$  is considered to be isotropic, but the excess luminosity  $\Delta L_* (\equiv L_* - L_{\text{crit}})$  is distributed into the radiation flux anisotropically as  $\Delta L_* (\mathcal{N} + 1) |\cos^{\mathcal{N}} \theta|$ , where  $\mathcal{N}$  characterizes the anisotropic degree and is set to  $\mathcal{N} = 4$  in our simulations (see also Ohsuga et al. 2005; Takeo et al. 2018). Therefore, the anisotropic degree of the flux is characterized as  $\mathcal{L}_*(\equiv \int \mathcal{L}_{*,\nu} d\nu) = L_{\text{crit}} + \mathcal{F}(\theta) \Delta L_*$  with a function of  $\mathcal{F}(\theta)$  defined by

$$\mathcal{F}(\theta) = \begin{cases} (\mathcal{N} + 1) |\cos^{\mathcal{N}} \theta| & (\Delta L_* > 0), \\ 1.0 & (\text{otherwise}). \end{cases} \quad (24)$$

It is worth mentioning that this anisotropic model injects radiation to the equatorial region ( $\theta \simeq \pi/2$ ) and the nonzero radiation flux through the equator affects the thermal properties of an accretion disk via IR re-emission from hot dust grains. In addition, RHD simulations performed by Ohsuga et al. (2005) suggest that a super-Eddington accreting disk transports a significant fraction of radiation energy through the equator via diffusion, and the luminosity is comparable to the Eddington value (although most radiation is collimated toward the poles). Therefore, we adopt  $L_{\text{crit}} = L_{\text{Edd}}$ .

### 2.4. Stellar Irradiation

Bulge stars are not only sources of external gravitational potential but also radiation sources associated with star formation activity. We here consider LW radiation and X-rays, which play an important role in determining the thermal and chemical properties of gas around the nuclear region. The LW and X-ray

radiation is mainly produced by short-lived massive stars and X-ray binaries, and their luminosities are proportional to the SFR. We assume that the bulge is composed of metal-poor stars with  $Z = 0.02 Z_\odot$  whose mass  $m_*$  follows a Salpeter initial mass function (IMF;  $1 \leq m_*/M_\odot \leq 100$ ), yielding the number flux of LW photons  $Q_{\text{LW}} \simeq 5.5 \times 10^{53} \text{ s}^{-1}$  ( $\text{SFR}/M_\odot \text{ yr}^{-1}$ ). Note that the number flux of LW radiation is lowered only by  $\simeq 15\%$  over  $5 \times 10^{-4} \leq Z/Z_\odot \leq 0.2$  (Schaerer 2003). Taking the mean energy of LW bands ( $h\nu_{\text{LW}} = 12.4 \text{ eV}$ ), the luminosity is calculated as  $L_{*,\text{LW}} = h\nu_{\text{LW}} Q_{\text{LW}} \simeq 1.1 \times 10^{43} \text{ erg s}^{-1}$  ( $\text{SFR}/M_\odot \text{ yr}^{-1}$ ). We also assume that the X-ray luminosity correlates with the SFR as seen in local star-forming galaxies:  $L_{*,\text{X}} \simeq 6.7 \times 10^{39} \text{ erg s}^{-1}$  ( $\text{SFR}/M_\odot \text{ yr}^{-1}$ ) in the 2–10 keV band (e.g., Grimm et al. 2003; Mineo et al. 2014).

We treat the stellar radiation field in the optically thin limit (note that the radiation flux produced from the central accreting BH dominates the stellar radiation flux at the vicinity of the BH within 1 pc). Assuming a spherically symmetric distribution of bulge stars, the radiation energy density at a distance of  $r$  from the center is given by

$$cE_{*,i}(r) = \int_0^r \epsilon_i(\hat{r}) \frac{\hat{r}^2}{r^2} d\hat{r} + \int_r^\infty \epsilon_i(\hat{r}) \frac{\hat{r}}{r} \ln \sqrt{\frac{\hat{r}+r}{\hat{r}-r}} d\hat{r}, \quad (25)$$

where the first and second terms in the right-hand side represent contributions from inside and outside the distance of  $r$ ,  $\epsilon_i(r)$  is the radiation emissivity at each cell

$$\epsilon_i(r) = \frac{L_{*,i}}{2\pi} \cdot \frac{r_c}{r(r+r_c)^3} \quad \text{for } i = \text{LW and X}, \quad (26)$$

where the functional form is given by the stellar mass distribution, and  $\rho_*(r) = \Delta\Phi_*(r)/(4\pi G)$ . Integrating Equation (25), we obtain

$$cE_{*,i}(r) = \frac{L_{*,i}}{4\pi r_c^2} \Xi(r/r_c), \quad (27)$$

where

$$\Xi(x) \equiv \frac{1}{(1+x)^2} + \int_x^\infty \frac{\ln(\frac{x_0+x}{x_0-x})}{(1+x_0)^3 x} dx_0. \quad (28)$$

The function of  $\Xi(x)$  is approximated as  $O(1)$  at  $x < 1$  and decreases as  $\propto x^{-2}$  at  $x \gg 1$ .

In this paper, we consider  $\text{H}_2$  photodissociation by LW radiation ( $\text{H}_2 + \gamma_{\text{LW}} \rightarrow 2\text{H}$ ),  $\text{H}^-$  photodetachment ( $\text{H}^- + \gamma_{\text{1eV}} \rightarrow \text{H} + \text{e}^-$ ) by photons with  $h\nu \simeq 1 \text{ eV}$ , and ionization/heating of H and He by X-rays with  $h\nu = 2 \text{ keV}$ . Those reaction rates are calculated in the same way as in Inayoshi & Tanaka (2015). For the  $\text{H}^-$  photodetachment rate, we set the minimum rate coefficient at a range of the effective temperatures of bulge stars ( $10^4 \text{ K} \leq T_{\text{eff}} \leq 10^5 \text{ K}$ ).<sup>9</sup> We also take into account secondary ionization by energetic electrons produced by primary X-ray ionization (Shull & van Steenberg 1985).

### 2.5. Boundary and Initial Conditions

We set a computational domain of  $r_{\text{min}} \leq r \leq r_{\text{max}}$  and  $\epsilon \leq \theta \leq \pi - \epsilon$ , where  $\epsilon = 0.001$  radian is set to avoid numerical

singularity at poles. We adopt logarithmically spaced grids in the radial direction and uniformly spaced grids in the polar direction. The number of the grid points is set to  $(N_r, N_\theta) = (250, 240)$ . For all of the simulations we conduct, the minimum and maximum radii are set to  $r_{\text{min}} = 0.1 \text{ pc}$  and  $r_{\text{max}} = 100 \text{ pc}$ .

We adopt the outflow boundary conditions at the innermost and outermost grid, where zero gradients across the boundaries are imposed on physical quantities in order to avoid spurious reflection of wave energy at the boundaries. We also impose  $v_r \leq 0$  at the inner boundary (i.e., inflowing gas from ghost cells is prohibited). At the poles, the reflective condition is imposed on the polar component of the velocity  $v_\theta$ . We set a density floor of  $n_{\text{min}} = 1 \text{ cm}^{-3}$  and a maximum radial velocity of  $v_{\text{max}} = 150 \text{ km s}^{-1}$ . This treatment allows us to avoid cells with a high Mach number ( $\gg 100$ ) in the outflowing regions near the inner and polar boundary.

As initial conditions, we consider a neutral gas cloud with a temperature of  $T = 10^4 \text{ K}$  and a spherically symmetric density profile with a flat core with the central density of  $n_c$  and an envelope following  $\propto r^{-2}$ ,

$$n(r) = \frac{n_c}{1 + (r/r_0)^2}, \quad (29)$$

where the core radius  $r_0$  is set so that the density profile becomes consistent with that of high-redshift protogalaxies obtained by cosmological simulations at  $r \gg r_0$ . Estimating the gas density at the outer boundary of the halo by the minimum-energy truncated isothermal sphere model as  $n_{\text{vir}} \simeq 0.07 \text{ cm}^{-3} [(1+z)/21]^3$  (Shapiro et al. 1999; Iliev & Shapiro 2001), the density profile outside the core is approximated as  $n(r) \simeq f_n n_{\text{vir}} (r/r_{\text{vir}})^{-2}$  or equivalently as

$$n(r) \simeq 2.5 \times 10^2 f_n T_{\text{vir},4} \left( \frac{r}{10 \text{ pc}} \right)^{-2} \text{ cm}^{-3}, \quad (30)$$

and thus the core radius is approximated as

$$r_0 \simeq 5 f_n^{1/2} T_{\text{vir},4}^{1/2} n_{c,3}^{-1/2} \text{ pc}, \quad (31)$$

where  $T_{\text{vir},4} = T_{\text{vir}}/(10^4 \text{ K})$ ,  $n_{c,3} = n_c/(10^3 \text{ cm}^{-3})$ , and  $f_n \sim O(1)$  is a numerical factor. We note that the density profile with  $f_n \simeq 4$  agrees with those of atomic-cooling halos with  $T_{\text{vir}} \simeq 10^4 \text{ K}$  obtained by cosmological simulations without star formation and stellar feedback (Wise et al. 2008; Shang et al. 2010; Regan et al. 2014). After a seed BH forms at the center of the halo, the density normalization becomes consistent with  $f_n \simeq 1$ .

In addition, star formation in the halo is modeled by assuming a conversion efficiency from gas into stars  $\epsilon_*$ . In our fiducial case, we adopt  $\epsilon_* = 0.05$  (e.g., Visbal et al. 2015), which is motivated by abundance matching and the observed UV luminosity function of galaxies at  $z \simeq 6$  (Bouwens et al. 2015). Note that the efficiency is calculated as the average value over time and scales in galaxies. Alternatively, we suppose that a star formation episode with a high value of  $\epsilon_*$  lasts within a few megayears in the nuclear region before SN explosions of massive stars begin to occur and regulate the star formation efficiency (SFE) in the bulge. According to numerical simulations that study star cluster formation from a giant molecular cloud with a size of 10–100 pc, the SFE becomes as high as  $\epsilon_* \gtrsim 0.2$ –0.3 when the initial gas surface

<sup>9</sup> While the  $\text{H}_2$  photodissociation rate hardly depends on  $T_{\text{eff}}$ , the  $\text{H}^-$  photodetachment rate increases with lower  $T_{\text{eff}}$  because photons with  $\simeq 1 \text{ eV}$  ( $\ll h\nu_{\text{LW}}$ ) contribute to the rate. With a realistic stellar spectrum for metal-poor galaxies (Inoue 2011), the  $\text{H}^-$  photodetachment rate boosts by a factor of  $\sim 20$  from that for  $T_{\text{eff}} = 10^5 \text{ K}$ .

**Table 1**  
Models Considered

Model	$M_\star (M_\odot)$	$T_{\text{vir}} \text{ (K)}$	$\epsilon_\star$	$n_c \text{ (cm}^{-3}\text{)}$	Transition	References
<b>Massive Halos<sup>a</sup></b>						
B7T5N4	$10^7$	$10^5$	0.05	$10^4$	Y	Section 3.2.1
B7T5N3.5	$10^7$	$10^5$	0.05	$10^{3.5}$	Y	Section 3.2.1
B7T5N3 (fiducial)	$10^7$	$10^5$	0.05	$10^3$	Y	Section 3.1
B7T5N2.5	$10^7$	$10^5$	0.05	$10^{2.5}$	Y	Section 3.2.1
B7T5N2	$10^7$	$10^5$	0.05	$10^2$	N	Section 3.2.1
B0T5N3	0	$10^5$	0.05	$10^3$	N	Section 3.2.2
B5T5N3	$10^5$	$10^5$	0.05	$10^3$	N	Section 3.2.2
B6T5N3	$10^6$	$10^5$	0.05	$10^3$	N	Section 3.2.2
B6.5T5N3	$10^{6.5}$	$10^5$	0.05	$10^3$	N	Section 3.2.2
B7T5N3-highSFE	$10^7$	$10^5$	0.5	$10^3$	Y	Section 3.2.3
<b>Normal Halos<sup>b</sup></b>						
B7T4N4	$10^7$	$10^4$	0.05	$10^4$	N	Section 3.2.4
B7T4N3	$10^7$	$10^4$	0.05	$10^3$	N	Section 3.2.4
B6T4N3	$10^6$	$10^4$	0.05	$10^3$	N	Section 3.2.4

**Notes.** Simulation runs and input parameters. Column (1) model ID, (2) initial bulge mass, (3) virial temperature of the host DM halo, (4) star formation efficiency, (5) initial gas density at the center, and (6) Y(N) indicates the cases where a transition to rapid accretion does (not) occur by the simulation termination at  $t = 4.0$  Myr (high-SFE case) and  $t = 3.5$  Myr (otherwise). Movies of these simulation are available at <https://www.youtube.com/playlist?list=PLqDrKvxmu0l4fyJ74u5ZYyQ8PmwuNZA32>.

<sup>a</sup> A massive dark-matter halo with  $M_h = 2 \times 10^9 M_\odot$  at  $z = 15$ .

<sup>b</sup> A normal atomic-cooling halo with  $M_h = 10^8 M_\odot$  at  $z = 10$ .

density is higher than  $\sim 10^3 M_\odot \text{ pc}^{-2}$  (Fukushima et al. 2020; Fukushima & Yajima 2021). Referring to those observational and theoretical studies, we assume  $f_n = f_0(1 - \epsilon_\star)$ , where  $f_0 = 1$  and  $\epsilon_\star = 0.05$  (fiducial case) and  $f_0 = 4$  and  $\epsilon_\star = 0.5$  (high SFE case). Following the definition of the SFE,  $\epsilon_\star$ , the SFR is approximated as

$$\text{SFR} = \frac{4\pi\epsilon_\star}{1 - \epsilon_\star} \rho(r) r^2 V_c, \\ \simeq 0.11 \epsilon_\star f_0 T_{\text{vir},4}^{3/2} M_\odot \text{ yr}^{-1}, \quad (32)$$

where  $V_c$  is the halo circular velocity. This SFR is used to estimate the emissivity of stellar irradiation (LW and X-rays) and to calculate the bulge growth in mass. Note that in most cases, the gas mass within  $r \simeq r_c$  for the given initial condition is lower than the total mass of newly forming stars.<sup>10</sup> Therefore, our star formation model implicitly assumes that the bulge growth is not led by in situ star formation but by efficient migration of stars formed at larger radii with morphological evolution owing to stellar relaxation (see also Appendix A).

The initial velocity field is set to  $(v_r, v_\theta, v_\phi) = (0, 0, j_{\text{in}}/R)$ , where  $R = r \sin \theta$  is the cylindrical radius. We assume that the initial specific angular momentum  $j_{\text{in}}(R)$  is proportional to the Keplerian velocity measured with the enclosed gas mass  $\mathcal{M}$  within a distance of  $R$ . Namely, we adopt  $j_{\text{in}}(R) = j_0 \sqrt{G\mathcal{M}R}$  and set  $j_0 = 0.3$ . The model assumption is motivated by the fact that the dynamics of a collapsing gas obeys a self-similar solution, and the rotational velocity in the accreting envelope where  $\rho \propto r^{-2}$  is a good fraction of the Keplerian velocity in agreement with hydrodynamical simulations of collapsing gas

in a DM halo (Abel et al. 2002; Yoshida et al. 2008; Inayoshi et al. 2014).

It is worth noting that if a uniform distribution of  $j_{\text{in}}$  is assumed, mass accretion within the well-defined centrifugal radius ( $\equiv j_{\text{in}}^2/GM$ ) is prevented without efficient viscous angular momentum transport. In this case, gas accretion through an isothermal, geometrically thin disk is stunted unless the centrifugal radius is smaller than  $\lesssim 1\%$  of the BH gravitational influence radius (Sugimura et al. 2018). As shown in Section 3, however, the initial condition adopted in our simulations leads to a wide range of angular momentum of the inflowing gas and thus allows for mass accumulation at various radii. Thus, the disk turns out dense enough to be gravitationally unstable, and additional viscosity given by the second term of Equation (15) is activated. As a result, the accretion flow overcomes the angular momentum barrier and feeds the central BH at super-Eddington rates (see Section 3.1).

An alternative way to alleviate the angular momentum problem is to consider the acceleration of the BH that would be expected in the presence of a dense (nuclear) star cluster. Gravitational scattering with the stars results in a jitter at the location of the BH, which leads to a cancellation of the angular momentum of the infalling gas onto the BH in its own rest frame. Alexander & Natarajan (2014) showed that this mechanism permits extended periods of super-Eddington accretion until the BH grows sufficiently to outweigh the star cluster (see also Natarajan 2021). The application to off-centered jittering BHs is left for future investigation, while in our simulations the location of the BH is fixed at the center but anomalous viscosity is responsible for angular momentum transport even without its cancellation.

## 2.6. Cases Considered

In Table 1, we summarize the models we consider in this paper. We consider two types of DM halos with different virial temperatures of  $T_{\text{vir}} \simeq 10^5 \text{ K}$  ( $M_h = 2 \times 10^9 M_\odot$  and  $z = 15$ ) and  $T_{\text{vir}} \simeq 10^4 \text{ K}$  ( $M_h = 10^8 M_\odot$  and  $z = 10$ ). The virial temperature of

<sup>10</sup> Although we do not consider the self-gravity of gas in our simulations, it would dominate the bulge gravity at the intermediate scale of  $\sim 0(10 \text{ pc})$  only in the early stage of the bulge formation where  $M_\star \lesssim 10^6 M_\odot$ . In this case, however, radiative feedback associated with BH accretion blows the gas outward, and then the gas self-gravity eventually becomes less important (see Section 3.2.2).



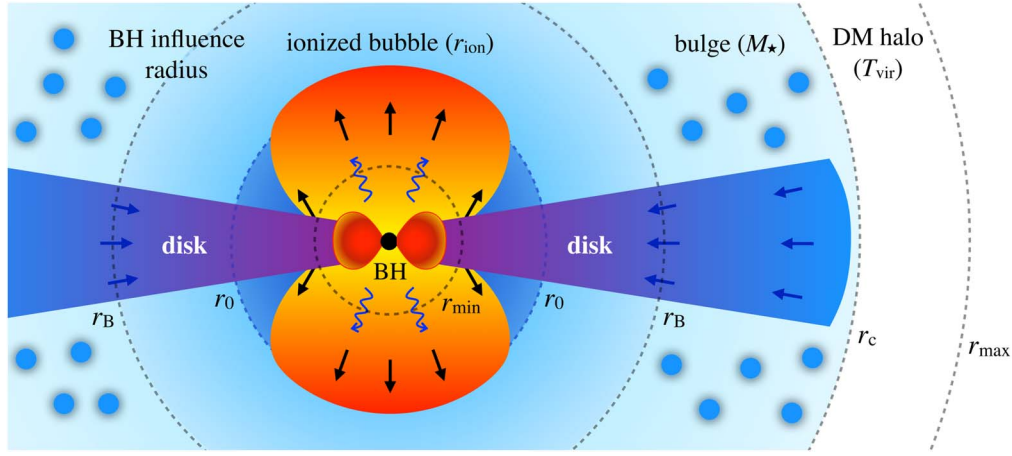


**Figure 1.** A schematic picture of accretion flows onto a massive BH embedded in a protogalactic bulge with a mass of  $M_*$  and DM halo with a virial temperature of  $T_{\text{vir}}$ . There are four characteristic scales: the core radius of the initial density distribution ( $r_0$ ), the BH gravitational influence radius ( $r_B$ ), the bulge core size ( $r_c$ ), and the size of ionized regions created by the radiating BH ( $r_{\text{ion}}$ ). The computational domain covers  $r_{\text{min}} \leq r \leq r_{\text{max}}$ , where those characteristic radii are well resolved.

the halo is calculated from the given values of  $M_h$  and  $z$  (see Equation (81) in Iliev & Shapiro 2001) by setting  $\mu = 0.6$  for  $T_{\text{vir}} \geq 10^4$  K (note that the mean molecular weight is calculated self-consistently by solving nonequilibrium thermochemistry in our simulations). The two cases are referred to as the “Massive Halo” model and “Normal Halo” model, respectively. In the former case, we consider a relatively massive DM halo because high-redshift quasar host galaxies form in rare, overdense regions of the universe at  $z > 6$ , and their progenitor halos would be likely as massive as our choice at higher redshifts when seed BHs form (Li et al. 2021b). The latter case corresponds to that of typical first galaxies where star formation is triggered by hydrogen atomic cooling (Bromm & Yoshida 2011).

We perform the 13 simulations shown in Table 1 with different bulge mass ( $M_* = 0, 10^5, 10^6, 10^{6.5}, \text{ and } 10^7 M_\odot$ ), initial gas density at the center ( $n_c = 10^2, 10^{2.5}, 10^3, 10^{3.5}, \text{ and } 10^4 \text{ cm}^{-3}$ ), and halo virial temperature ( $T_{\text{vir}} = 10^4$  and  $10^5$  K). In all of the simulations, we adopt the initial BH mass to  $M_{*,0} = 10^5 M_\odot$ . The SFE and the initial density normalization are assumed to be  $\epsilon_* = 0.05$  and  $f_0 = 1$ , respectively, for most of the cases. To see the impact of their parameter choice, we additionally consider a case (B7T5N3-highSFE), where a higher SFE of  $\epsilon_* = 0.5$  and  $f_0 = 4$  are set.

In Figure 1, we summarize the characteristic physical scales that determine the properties of accretion flows onto a seed BH embedded in a protogalaxy. In our case, the typical value of the BH gravitational influence radius (the so-called Bondi radius) is given by

$$r_B \equiv \frac{GM_*}{c_s^2} \simeq 6.4 \left( \frac{M_*}{10^5 M_\odot} \right) \left( \frac{T}{10^4 \text{ K}} \right)^{-1} \text{ pc}, \quad (33)$$

for neutral gas ( $\mu = 1.22$ ) and  $r_{B,\text{ion}} \simeq 0.32 \text{ pc} (M_*/10^5 M_\odot) (T/10^5 \text{ K})^{-1}$  for ionized gas ( $\mu = 0.6$ ). We note that both of the scales are well resolved in our simulations (i.e.,  $r_{\text{min}} < r_{B,\text{ion}} < r_B < r_{\text{max}}$ ). This indicates the distance from the BH within which the gravitational energy dominates over the thermal energy of the gas and thus gas accretion begins to occur unless BH feedback plays an important role. In reality, however, when the BH grows via mass accretion, the accreting flow releases its gravitational energy as radiation, which heats the surrounding gas and forms an ionized bubble with a size of  $r_{\text{ion}}$ . In the

intermediate region, stars form a galactic bulge component with a total mass of  $M_*$  and a half-mass-radius of  $R_e = (1 + \sqrt{2})r_c \simeq 16 \text{ pc} (M_*/10^7 M_\odot)^{0.47}$ . For both the “massive” and “normal” halo cases, the halo virial radii are  $r_{\text{vir}} \simeq 1.6 \text{ kpc}$  and  $0.9 \text{ kpc}$ , respectively. Therefore, our computational domain covers the interior of the host DM halo ( $r_{\text{max}} \simeq 0.1 r_{\text{vir}}$ ).

### 3. Results

#### 3.1. Fiducial Case

We first discuss the fiducial case where a BH with  $M_* = 10^5 M_\odot$  is embedded in a dense gas cloud with central density  $n_c = 10^3 \text{ cm}^{-3}$  hosted in a stellar bulge with initial mass  $M_* = 10^7 M_\odot$  hosted in a massive DM halo with  $M_h = 2 \times 10^9 M_\odot$  at  $z = 15$  (the corresponding virial temperature is  $T_{\text{vir}} \simeq 10^5 \text{ K}$ ). The SFE is set to  $\epsilon_* = 0.05$ .

Figure 2 shows the time evolution of the accretion rate  $\dot{M}$  (solid curve). As reference values, the Eddington accretion rate  $\dot{M}_{\text{Edd}}$  and the critical rate for the onset of hyper-Eddington accretion ( $\simeq 500 \dot{M}_{\text{Edd}}$ ; Inayoshi et al. 2016) are shown with dashed curves. At the early stage of  $t < 1.6 \text{ Myr}$ , the mass accretion proceeds episodically. While the accretion rate exceeds the Eddington value during those burst phases, the long-term average rate is  $\simeq \dot{M}_{\text{Edd}}$  due to radiative feedback associated with BH feeding. At  $t \simeq 1.6 \text{ Myr}$ , the mass accretion rate abruptly rises and reaches  $\dot{M} \simeq 10 M_\odot \text{ yr}^{-1}$ , which corresponds to  $\simeq 2.5 \times 10^3 \dot{M}_{\text{Edd}}$ . After the peak, the rate gradually decreases with time, but the super-Eddington accretion phase lasts until  $t \simeq 3 \text{ Myr}$ . Note that the BH mass is  $\simeq 6.3 \times 10^5 M_\odot$  at the end of the simulation. The overall behavior of the accretion rate is consistent with those found in previous RHD simulations where the BH is not embedded in the external gravitational potential composed of stars and DM (Inayoshi et al. 2016; Takeo et al. 2018, 2020; Park et al. 2020; Toyouchi et al. 2021).

Figure 3 presents the distribution of the gas density in the domain of  $0 \leq x \leq 8 \text{ pc}$  and  $|z| \leq 6 \text{ pc}$  at six different elapsed times (phases (a)–(f) of Figure 2). In each panel, the location of the ionization front where the neutral fraction is  $x_{\text{HI}} = 0.95$  (thin contours), and the velocity vectors are overlaid. Figure 4 presents the radial profiles of the gas density (top), temperature (middle), and velocity (bottom) along the equator ( $\theta = 90^\circ$ ; left



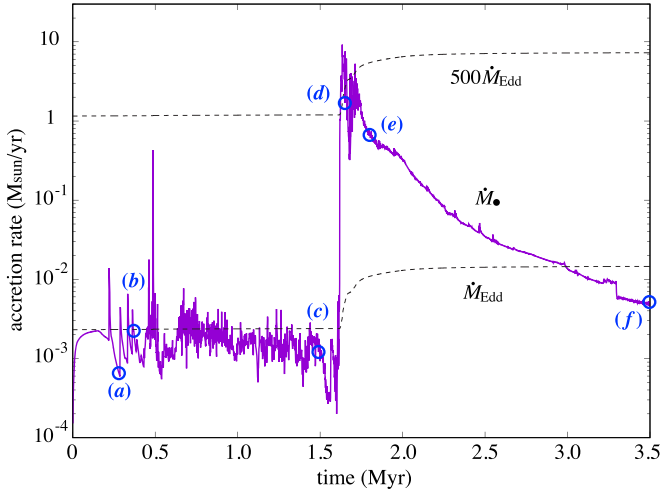


**Figure 2.** Time evolution of the gas accretion rate onto a massive BH with an initial mass of  $M_{\bullet} = 10^5 M_{\odot}$  embedded in a dense gas cloud with a central density of  $n_c = 10^3 \text{ cm}^{-3}$  hosted in a stellar bulge with  $M_{\star} = 10^7 M_{\odot}$  and a massive DM halo with a virial temperature of  $T_{\text{vir}} \simeq 10^5 M_{\odot}$  (model: B7T5N3). The dashed curves show the Eddington accretion rate  $\dot{M}_{\text{Edd}}$  and the critical rate for the onset of rapid mass accretion ( $\sim 500 \dot{M}_{\text{Edd}}$ ) obtained in previous RHD simulations (Inayoshi et al. 2016). Open circles mark the six epochs at which we show the density and temperature distributions in Figure 3 and radial profiles of the physical quantities in Figure 4.

panels) and the pole ( $\theta = 0^\circ$ ; right panels), respectively. In the bottom panels, we show the rotational velocity along the equator and radial velocity along the polar direction, respectively. Note that the radial profiles at phase (f) are not shown because they are similar to those at phase (e), except that the shock front of the polar outflow moves forward. This indicates that the disk properties are in a quasi-steady state, although the net accretion rate onto the BH gradually decreases.

At the early stage of  $t < 0.3 \text{ Myr}$ , the accreting BH emits nearly isotropic radiation and creates an ionizing bubble. The prolate shape of the bubble is caused by angular momentum of the inflowing gas with a lower density near the pole and by anisotropic radiation produced when the BH feeding rate exceeds the Eddington value in a short period. While the size of the ionizing bubble is initially maximized at  $r_{\text{ion}} \sim 30 \text{ pc}$ , it shrinks to  $\sim 3 \text{ pc}$  by phase (a) owing to efficient radiative recombination of the gas surrounding the Eddington-limited radiating BH. As a result, the equatorial inflow of neutral gas penetrates into the interior of the BH gravitational influence radius of  $r_B \simeq 8 \text{ pc}$  for neutral gas with  $T \simeq 8000 \text{ K}$  (see the left panels in Figure 4). The inflow with strong ram pressure leads to fragmentation of the shell of the ionized bubble. Previous studies also found that collapse of an ionized region surrounding the accreting BH is an essential process to trigger the accretion transition (Inayoshi et al. 2016; Sakurai et al. 2016; Toyouchi et al. 2019, 2021). However, we note that gas rotation, anisotropic radiation, and dust obscuration moderate the propagation of ionizing radiation to the equatorial region and thus *do* promote the transition (see also Takeo et al. 2018, 2020).

At  $t \simeq 0.35 \text{ Myr}$  (phase (b)), intense inflows of neutral gas feed the nuclear scale within  $\sim 2 \text{ pc}$ , but the BH feeding rate does not increase at the same moment. This is primarily because the inflowing gas with angular momentum forms a rotationally supported disk, and the rotational velocity exceeds the Keplerian value at  $r \sim 2 \text{ pc}$  (see the left-bottom panel in Figure 4), where the inflow speed through the disk slows down

significantly. In addition, the outward radiation force exerted through electron scattering, absorption of UV radiation by atomic bound-free transitions and dust grain, and re-emission of IR radiation from heated dust prevent the inflowing gas from feeding the BH at rates of  $\gtrsim \dot{M}_{\text{Edd}}$  (Toyouchi et al. 2019). Meanwhile, the ionized regions become as small as  $r_{\text{ion}} \simeq 0.3 \text{ pc}$ , and the inflow from larger radii accumulates mass in the nuclear region (phase (c); see Figure 3 and the left panels in Figure 4).

At the late stages of  $t \gtrsim 1.6 \text{ Myr}$  (phase (d)), the disk becomes opaque to UV by dust, and the inner-edge of the dense dusty disk reaches the central cell with  $r_{\text{min}} = 0.1 \text{ pc}$ . Meanwhile, the mid-plane density approaches the profiles of  $\rho_{\text{crit}} = \Omega_K^2 / (\pi G)$  (the dashed line in the top-left panel of Figure 4), where the Toomre’s  $Q$  parameter is nearly set to unity within the disk. Since the disk feeds the BH at rates exceeding the Eddington value, the radiation flux from the center blows the gas away and launches strong outflows toward the polar regions at velocities of  $v_{\text{out}} \simeq 150 \text{ km s}^{-1}$ , which is significantly faster than the escape velocity from the system (see Figure 3). In phase (e), the radiation-driven outflow collides with the inflowing gas and creates bipolar low-density cavities surrounded by a dense shell (see the right panels in Figure 4). As a result, the emergent UV radiation begins to heat the disk surface and drives thermally driven outflows. Although the radiation/mechanical feedback effect suppresses the mass supply from larger radii, the dense accretion disk coexists with outflows and feeds the central BH at super-Eddington rates  $\gtrsim \dot{M}_{\text{Edd}}$  until  $t \simeq 3.5 \text{ Myr}$  (phase f), when the simulation terminates.

### 3.2. Parameter Dependence

Next, we investigate the dependence of the result on the model parameters: (1) the central density  $n_c$ , (2) the bulge mass  $M_{\star}$ , (3) the SFE,  $\epsilon_{\star}$ , and (4) the halo virial temperature  $T_{\text{vir}}$ .

#### 3.2.1. Central Density $n_c$

In Figure 5, we present the time evolution of the BH accretion rate (left) and the mass accreted onto the BH (right) with different values of the central density for the initial conditions. The transition to rapid accretion tends to occur earlier with higher values of  $n_c$ . This is because the size of the ionized region surrounding the BH becomes smaller due to efficient recombination and thus collapse of the compact ionized region triggers the BH feeding in a shorter dynamical timescale. Although this trend holds for  $n_c \geq 10^3 \text{ cm}^{-3}$ , the accretion transition for the lowest-density case ( $n_c = 10^{2.5} \text{ cm}^{-3}$ ) occurs earlier than that for the fiducial case due to the stochastic nature of mass accretion through filamentary structures and a compact disk at  $\sim 1 \text{ pc}$  (see phase (b) in Figure 3). Moreover, the two cases ( $n_c = 10^{2.5}$  and  $10^{3.5} \text{ cm}^{-3}$ ) show accretion bursts twice by the end of the simulations. In those cases, the vertical oscillation of the accretion disk after its formation promotes mass loading into radiation-driven outflows, and the net accretion rate through the disk decreases quickly with time. However, as a result of weak radiative feedback, continuous mass supply from large radii triggers the second accretion burst within  $\sim 1 \text{ Myr}$ . In spite of the stochastic nature of mass accretion, the gas mass accreted onto the BH reaches similar values of  $\Delta M_{\bullet} \simeq (3\text{--}6) \times 10^5 M_{\odot}$ , which is substantially higher than that expected under the Eddington growth (dashed curve). We note

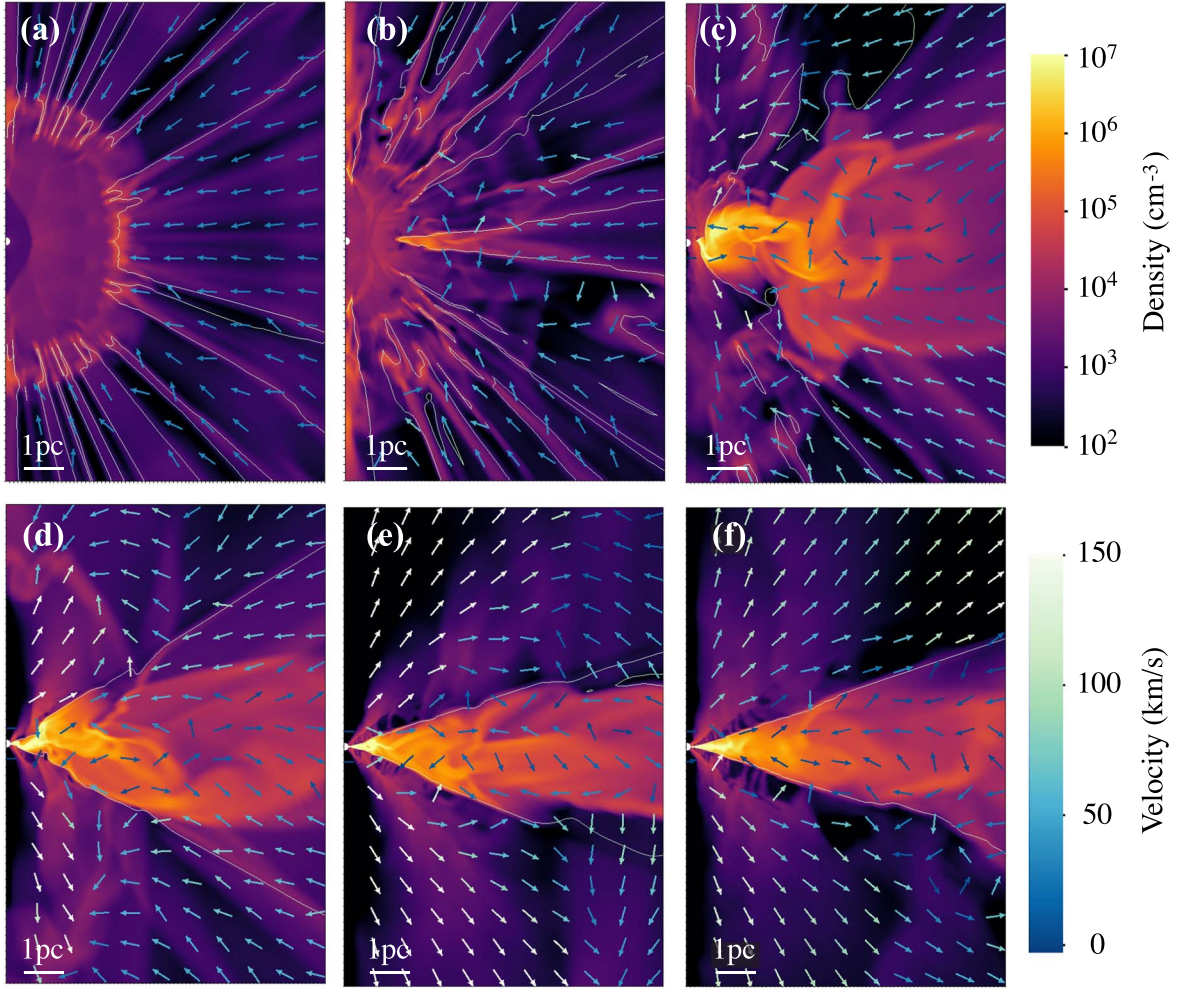


**Figure 3.** Distribution of the gas density for the fiducial case at the six elapsed times denoted by open circles in Figure 2. In each panel, the location of the ionization front where the neutral fraction is  $x_{\text{HI}} = 0.95$  (thin contours), and the velocity vectors are overlaid. In the first two panels, (a) and (b), the velocity vectors with  $|\mathbf{v}| \geq 30 \text{ km s}^{-1}$  are shown. At the early stage ( $t < 1.6 \text{ Myr}$ ; phases (a)–(c)), the intense inflows of neutral gas lead to collapse of the ionized region and form a dense gaseous accretion disk within the BH influence radius. In the late stage ( $t > 1.6 \text{ Myr}$ ; phases (d)–(f)), the disk feeds the BH at rates of  $\gg \dot{M}_{\text{Edd}}$ , and the bipolar outflows driven by radiation decrease the gas supplying rate from larger radii. Movies of this simulation are available at <https://www.youtube.com/playlist?list=PLQDrKvxmu0l4fyJ74u5ZYyQ8PmwuNZA32>.

that the accreted mass is comparable to that contained within the gaseous core in the initial state ( $r \lesssim r_0$ ).

It is worth mentioning that all of the cases in Figure 5 experience the transitions to rapid accretion exceeding the Eddington rate. As described in Figure 4, the transition is induced by continuous accretion of neutral gas whose inward ram pressure pushes the ionization front (hereafter, I-front). In Section 4, we quantify the conditions required for the onset of rapid mass accretion. On the contrary, when the central density is lower than  $n_c \sim 10^2 \text{ cm}^{-3}$  (model: B7T5N2), the ionized region quickly reaches the core radius  $r_0$ . Since the density follows  $\rho \propto r^{-2}$  outside the core, the I-front expands farther at speeds faster than the sound speed of ionized gas without disturbing the density structure (the so-called R-type I-front), and the entire cloud is ionized (e.g., Kitayama et al. 2004; Whalen & Norman 2006). In this case, therefore, the transition to rapid mass accretion does not occur.

### 3.2.2. Bulge Mass $M_*$

Figure 6 shows the time evolution of the mass accretion rate with four different bulge masses at  $0 \leq M_*/M_\odot \leq 10^7$ . In

Figure 7, we also present the density distribution for the two cases of  $M_* = 0$  (no bulge) and  $10^{6.5} M_\odot$  around the epochs when the simulations terminate, respectively.

Without the bulge component, the accretion rate shows multiple bursts with a period of  $\simeq 0.6 \text{ Myr}$ , and the time-averaged rate is significantly below the Eddington value; namely  $\langle \dot{M} \rangle \simeq 0.2 \dot{M}_{\text{Edd}}$ . In this case, the I-front initially propagates up to  $\sim 25 \text{ pc}$  and heats the ambient gas outside the BH influence radius  $r_B \simeq 5 \text{ pc}$ . Within the hot ionized gas, the BH’s gravity accelerates the inflow within a new sonic point in the hot region ( $\simeq 0.4 \text{ pc}$  for  $T \simeq 10^5 \text{ K}$ ), while the gas pressure (and partially the radiation pressure force) pushes the gas outwards at  $r \gtrsim 1 \text{ pc}$ , and the mass accretion rate is suppressed. In the quiescent phases, although the gas is in thermal-pressure equilibrium against the BH gravity, the mass depletion owing to BH feeding reduces the outward pressure gradient force. As a result, the dense shell surrounding the ionized gas accretes to the BH and leads to burst-like accretion again. The overall behavior of mass accretion is consistent with previous RHD simulations where the BH is assumed to be embedded in a uniform density distribution (e.g., Ciotti & Ostriker 2001; Milosavljević et al. 2009; Park & Ricotti 2011, 2012; Inayoshi et al. 2016; Park et al. 2017). In our case, where the gas density

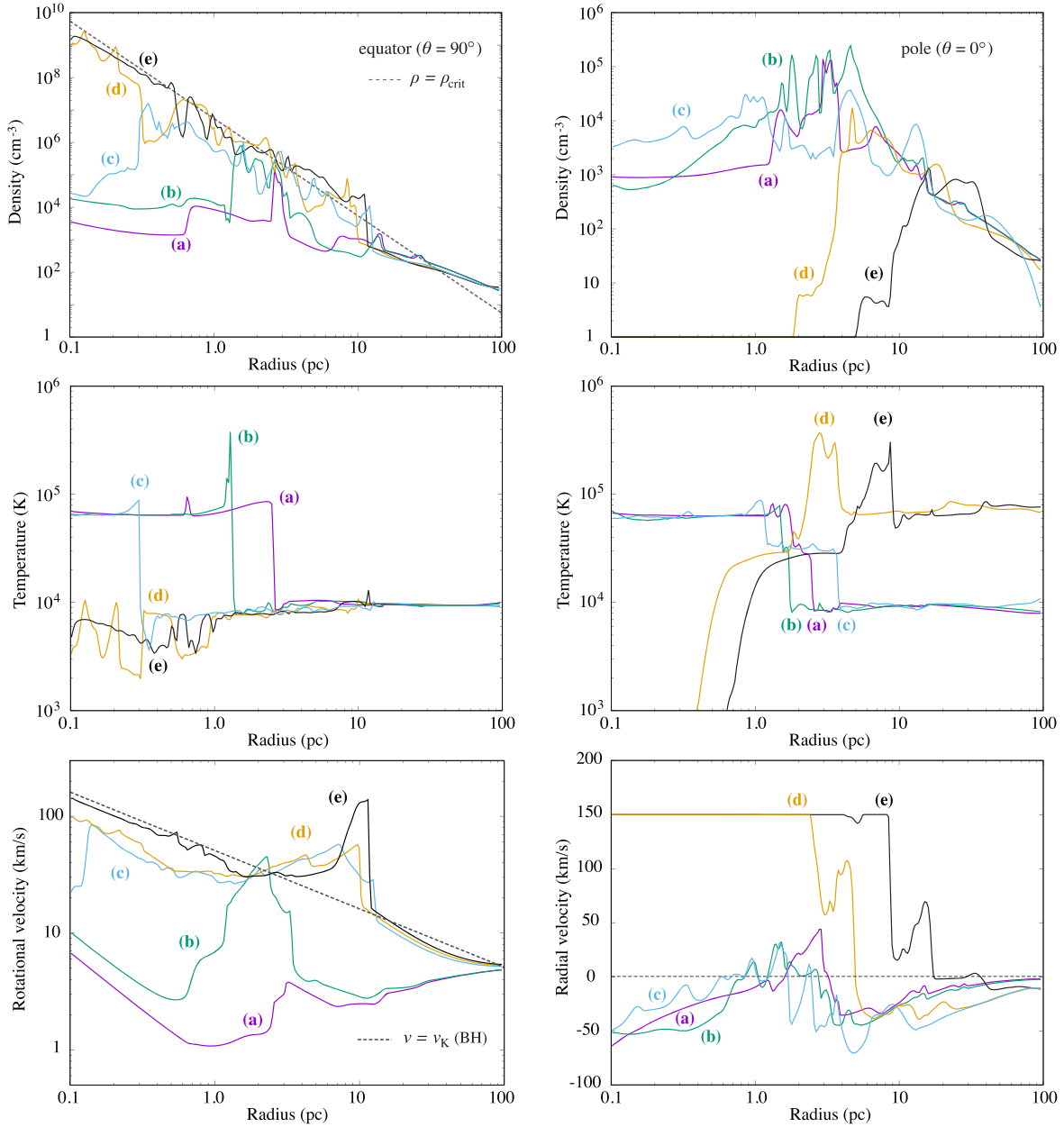


**Figure 4.** Radial structure of the gas density (top), temperature (middle), velocity (bottom) along the equator ( $\theta = 90^\circ$ ; left-hand panels) and pole ( $\theta = 0^\circ$ ; right-hand panels). The bottom panels present the rotational velocity along the equator and radial velocity along the polar direction, respectively. In each panel, we show the profiles at different epochs during and after the transition:  $t = 0.28$  Myr (phase (a); purple),  $0.35$  Myr (phase (b); green),  $1.5$  Myr (phase (c); blue),  $1.65$  Myr (phase (d); yellow), and  $1.8$  Myr (phase (e); black). In the top-left and bottom-left panels, we overlay the critical density (see the viscous model below Equation (15)) and the Keplerian velocity for  $M_* = 6 \times 10^5 M_\odot$ .

decreases outward, the I-front continues to expand during the multiple episodes of burst-like accretion and reaches  $\gtrsim 40$  pc by  $t \simeq 3.5$  Myr.

With the bulge mass increasing, the episodic behavior of mass accretion ceases and the time-average rate increases because the gas density and mass inflow rate are enhanced within the additional bulge-gravitational potential. When the bulge mass is lower than  $M_* < 10^7 M_\odot$ , however, the ionized region continues to expand and heats the surrounding gas in the same way as in the case without a bulge. Note that this statement is still valid if the self-gravity of gas would be taken into account in our simulations, since the total gas mass in the domain is lower than  $10^7 M_\odot$ . As a result, the transition to rapid mass accretion does not occur by the end of the simulation. Since the freefall velocity at  $r \simeq 50$  pc is  $\sim 20 \text{ km s}^{-1}$  (the

enclosed mass is dominated by the bulge), the transition could not occur within another  $\sim 2.5$  Myr even if all of the radiative output turned off.

In summary, the size of the expanding I-front determines the nature of mass accretion onto the BH, and the formation/acceleration of neutral-gas inflows from larger radii is a key process to trigger the accretion transition. Based on those findings, we give a simple analytical argument for the conditions required for the transition in Section 4.

### 3.2.3. Star Formation Efficiency $\epsilon_*$

Figure 8 shows the time evolution of the mass accretion rate (solid), the Eddington accretion rate (dotted), and the BH-to-bulge mass ratio of  $M_*/M_*$  (dashed) for the case with a high



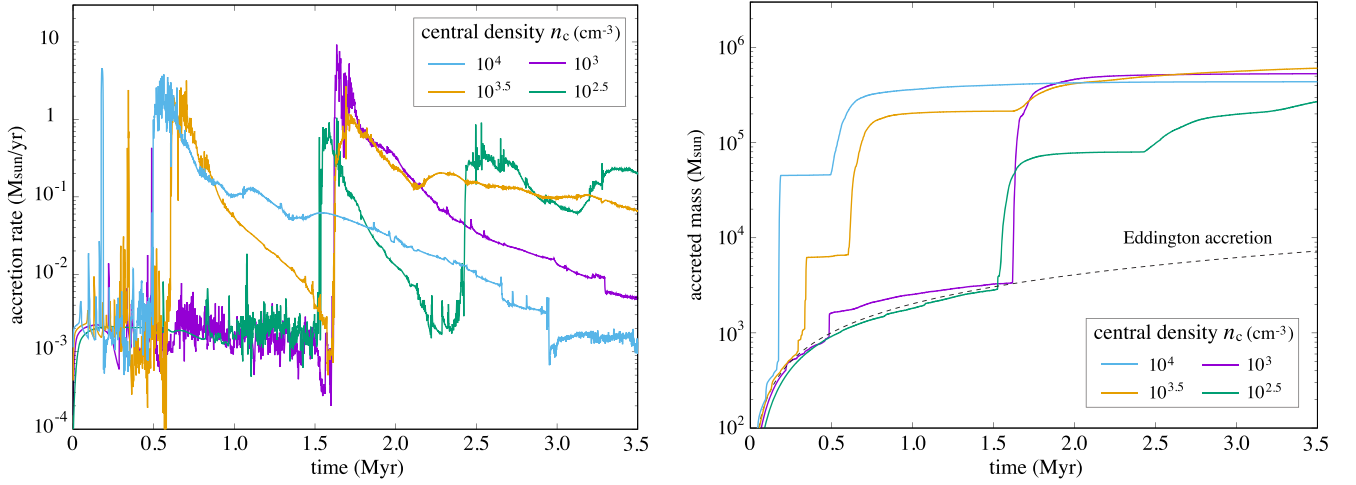


**Figure 5.** Time evolution of the BH accretion rate (left) and the mass accreted onto the BH (right) with different values of the central density for the initial conditions;  $n_c = 10^4 \text{ cm}^{-3}$  (cyan),  $10^{3.5} \text{ cm}^{-3}$  (orange),  $10^3 \text{ cm}^{-3}$  (purple; fiducial case), and  $10^{2.5} \text{ cm}^{-3}$  (green). The transition of rapid accretion tends to occur earlier with higher values of  $n_c$ . In spite of the stochastic nature of mass accretion, the mass accreted onto the BH reaches similar values of  $\Delta M \simeq (3 - 6) \times 10^5 M_\odot$ , which is substantially higher than that expected under the Eddington growth (dashed curve).

SFE ( $\epsilon_* = 0.5$ ; B7T5N3-highSFE). The overall behavior of the accretion rate is consistent with the cases with the lower SFE, as shown in Figure 5. Compared to the fiducial case, the transition to rapid accretion occurs earlier because a larger amount of gas is accumulated within the gravitational influence radius of the fast growing bulge. With the high SFR, intense stellar radiation heats the gas surrounding the BH, but efficient radiative cooling keeps the gas neutral. As a result, the attractive gravitational force by the massive bulge is more important than the negative feedback effect caused by the stellar irradiation. In addition, the BH-to-bulge mass ratio evolves substantially within  $\sim 3 \text{ Myr}$ , and the ratio reaches  $\sim 0.04$  at the end of the simulation. This mass ratio is  $\sim 10$  times higher than the BH-galaxy correlation seen in the local universe (Kormendy & Ho 2013) and is consistent with those of bright quasars at  $z > 6$  (see more discussion in Section 5.2).

#### 3.2.4. Virial Temperature of Host DM Halos $T_{\text{vir}}$

We examine three cases of BH accretion in a typical atomic-cooling halo with a virial temperature of  $T_{\text{vir}} = 10^4 \text{ K}$  (see Table 1). For all of the cases, the I-front quickly expands and reaches the outermost radius of the computational domain. Since the I-front is R-type, the density profile does not change from the initial distribution except within 1 pc, where the BH gravitational force pulls the ionized gas toward the center and increases the density as  $\rho \propto r^{-3/2}$ . However, the accretion rate of the ionized gas is limited to the Eddington owing to the outward radiation force via electron scattering. Due to the self-regulated nature of BH radiative outputs, the gas ejection from the halo takes place in a relatively slow manner, unlike stellar irradiation and supernova feedback with given feedback energy (e.g., Kitayama et al. 2004; Kitayama & Yoshida 2005). Overall, the stunted growth of seed BHs in “normal” atomic-cooling halos is consistent with previous studies that use cosmological hydrodynamical simulations (Habouzit et al. 2017; Latif et al. 2018), although our simulations focus on the early stage of the bulge formation without including SN feedback.

#### 3.3. Radiative Luminosity of Rapidly Accreting Seed BHs

In the left panel of Figure 9, we present the time evolution of the radiative luminosity produced by a rapidly accreting seed BH for the high-SFE case (purple), the fiducial case (green), and the high-density case with  $n_c = 10^{3.5} \text{ cm}^{-3}$  (cyan). Here, the radiative luminosity is calculated by using Equation (23) as a function of the BH feeding rate. We note that in general, this luminosity is not the one we observe but that injected through the innermost cells of the simulation. The two values are almost identical when and after the accretion transition occurs, because intense radiation ionizes the surrounding gas and blows the gas farther away, reducing the amount of absorbers along the line of sight. However, in the early stage before the accretion transition, the injected radiation flux is attenuated by the surrounding neutral gas and dust to some degree. When the mass accretion increases during the transition, the radiative luminosity also rises and reaches  $L_* \simeq (0.3 - 1.2) \times 10^{45} \text{ erg s}^{-1}$ , corresponding to  $L_*/L_{\text{Edd}} \sim 4 - 16$ . We note that the luminosity of the accreting BH for each case substantially dominates that of the host galaxy; namely, the LW luminosities we assume as sources of stellar feedback are  $1.9 \times 10^{42} \text{ erg s}^{-1}$  (fiducial case) and  $7.6 \times 10^{43} \text{ erg s}^{-1}$  (high-SFE case), respectively.

With our spectral model for the injected radiation (see Equation (22)),  $\sim 55\%$  of the total radiation energy is emitted as photons with  $h\nu < h\nu_0 = 10 \text{ eV}$  (the rest-frame wavelength is  $\lambda_0 = 0.124 \mu\text{m}$ ), which are not absorbed significantly by the intergalactic media. The specific radiation luminosity at  $\nu = \nu_0$  is calculated by  $L_{\nu_0} = L_0 = L_*/(3.3\nu_0)$ . As an example, we consider that a seed BH is accreting in a protogalaxy at  $z \simeq 15$  (the luminosity distance is  $D_L \simeq 167 \text{ Gpc}$ ). In this case, the wavelength of the rest-frame  $h\nu_0 = 10 \text{ eV}$  photons is redshifted to  $\lambda_{\text{obs}} \simeq 1.98 \mu\text{m} [(1+z)/16]$ , and the observed radiative flux is calculated via

$$F_{\nu_{\text{obs}}} = \frac{(1+z)}{4\pi D_L^2} \cdot \frac{L_{\text{Edd}} + \mathcal{F}(\theta_{\text{obs}})\Delta L_*}{3.3 \nu_0}, \quad (34)$$

where  $\nu_{\text{obs}} = \nu_0/(1+z) [= c/\lambda_{\text{obs}}]$  is the observed frequency,  $\Delta L_* = L_* - L_{\text{Edd}}$ , and the anisotropic degree of the flux is characterized by the function of  $\mathcal{F}(\theta_{\text{obs}})$  (see Equation (24)).

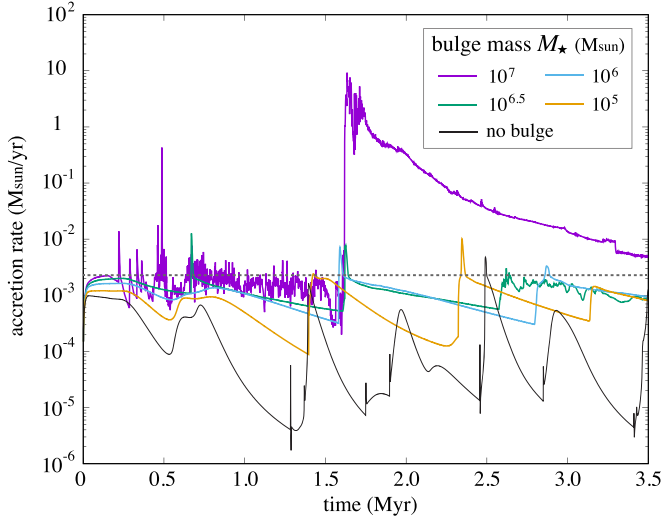


**Figure 6.** Time evolution of the mass accretion rate onto the BH with different values of the bulge mass;  $M_* = 10^7 M_\odot$  (purple),  $10^6 M_\odot$  (cyan),  $10^5 M_\odot$  (orange),  $10^4 M_\odot$  (green), and no bulge (black). The transition to rapid accretion phases occurs when the bulge mass is as high as  $M_* = 10^7 M_\odot$ , which corresponds to  $\sim 100 M_\odot$  (see also the discussion in Section 4). As a reference, the Eddington accretion rate for  $M_* = 10^5 M_\odot$  is overlaid (horizontal dashed line), above which anisotropic radiation is produced.

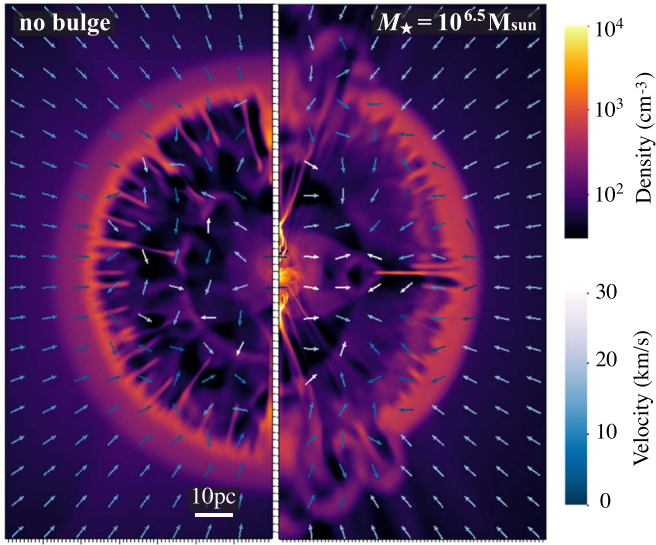


**Figure 7.** Distribution of the gas density for the case without bulge stars (left) and with the bulge of  $M_* = 10^{6.5} M_\odot$  (right) at the end of those simulations. The arrows present the velocity vectors. In both cases, the accreting BH is surrounded by an expanding ionized region, and thus rapid inflows of neutral gas onto the central BH are not observed.

The right panel of Figure 9 presents the radiative flux at  $\lambda_{\text{obs}} = 1.98 \mu\text{m}$  emitted from the accreting BH in a protogalaxy at  $z = 15$ , seen from a viewing angle of  $\theta_{\text{obs}} = 30^\circ$ . We note that the  $x$ -axis is the time at the source rest frame (the redshift effect is not considered). After the transition of mass accretion, the observed flux becomes as high as  $\sim 0.01\text{--}0.2 \mu\text{Jy}$ , corresponding to  $m_{\text{AB}} \simeq 29\text{--}26$  mag. For comparison, we overlay the S/N = 10 detection limit of JWST/NIRCam imaging with the F200W filter at  $1.755 \leq \lambda_{\text{obs}}/\mu\text{m} \leq 2.226$  in a 10 ks exposure time ( $m_{\text{AB}} \simeq 29$  mag denoted by the dashed line; Rieke et al. 2019).<sup>11</sup>

<sup>11</sup> <https://jwst-docs.stsci.edu/jwst-near-infrared-camera/nircam-instrumentation/nircam-filters>

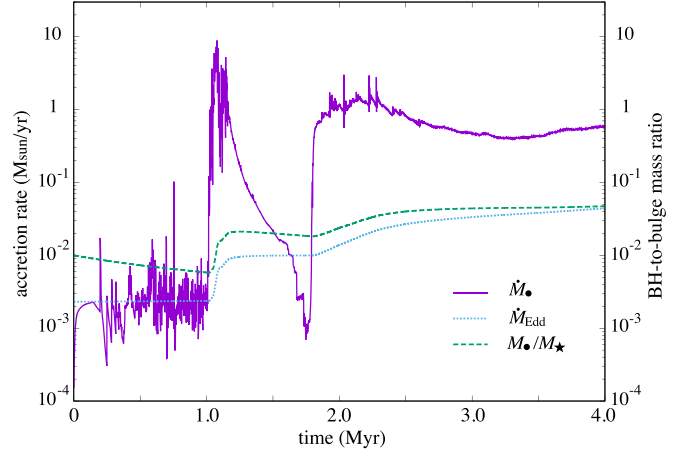


**Figure 8.** Time evolution of the mass accretion rate onto a BH (solid), the Eddington accretion rate (dotted), and the BH-to-bulge mass ratio (dashed) for the case with a high SFE ( $\epsilon_* = 0.5$  and  $f_0 = 4$ ). In this case, both the BH and bulge evolve within the simulation time, and the mass ratio reaches  $M_\bullet/M_* \simeq 0.04$ , which is consistent with those of bright quasars at  $z > 6$  (see also Section 5.2).

For all of the cases, the radiation flux can be detectable (i.e.,  $m_{\text{AB}} < 29$  mag) in durations of  $\Delta t \gtrsim 2$  Myr at the source rest frame. The corresponding duty cycle is  $f_{\text{duty}} \sim 7\%$  of the cosmic time duration when the redshift changes by  $\Delta z = \pm 0.5$ . Note that the host galaxy is as bright as  $\sim 0.02 \mu\text{Jy}$  ( $m_{\text{AB}} \gtrsim 28$  mag) for the high-SFE case and would not be a serious contamination for hunting seed BHs but rather be a detectable extended source with JWST.

We finally estimate the number of rapidly accreting seed BHs detectable within a JWST/NIRCam field of view (FoV =  $9.7 \text{ arcmin}^2 = 0.0027 \text{ deg}^2$ ) as

$$N_{\text{det}}^{\text{JWST}} = f_{\text{duty}} \mathcal{N}_{\text{h,seed}} \Delta V_c(z) \frac{\Delta \Omega_{\text{obs}}}{4\pi} \simeq 1.1 \left( \frac{f_{\text{duty}}}{0.1} \right) \left( \frac{\Delta \Omega_{\text{obs}}}{10 \text{ FoV}} \right) \left( \frac{\mathcal{N}_{\text{h,seed}}}{10^{-4} \text{ cMpc}^{-3}} \right), \quad (35)$$

where  $\Delta \Omega_{\text{obs}}$  is the observed solid angle, and  $\mathcal{N}_{\text{h,seed}}$  is the comoving number density of DM halos that host growing seed BHs. Here, we consider only the BH luminosity, because the seed BHs outshine their host galaxies. The number density of DM halos with  $M_{\text{h}} \geq 2 \times 10^9 M_\odot$  at  $z = 15$  is estimated as  $\mathcal{N}_{\text{h}} \simeq 2.5 \times 10^{-3} \text{ Mpc}^{-3}$ . Therefore, if  $\gtrsim 4\%$  of those DM halos at  $z = 15$  contain seed BHs, we are able to detect one rapidly accreting seed BH by JWST in its 10 fields of view. We also note that the detectability depends on the viewing angle  $\theta_{\text{obs}}$ . Namely, the direct component of the BH radiation flux is reduced by one order of magnitude for observers with  $|\theta_{\text{obs}} - 90^\circ| \lesssim 20^\circ$  (i.e., a nearly edge-on view); otherwise, it is detectable with JWST.

Deep imaging surveys by the RST will also enable us to hunt for a larger number of rapidly accreting BHs in the early universe. Assuming the survey area is as large as  $\Delta \Omega_{\text{obs}} \simeq 40 \text{ deg}^2$  and the limiting magnitude is  $m_{\text{AB}} \simeq 28\text{--}29$  with the F184 filter at  $1.68 \leq \lambda_{\text{obs}}/\mu\text{m} \leq 2.00$  as planned in Akeson et al. (2019), the expected number of detected seed BHs would be

$$N_{\text{det}}^{\text{RST}} \simeq 1.6 \times 10^3 \left( \frac{f_{\text{duty}}}{0.1} \right) \left( \frac{\Delta \Omega_{\text{obs}}}{40 \text{ deg}^2} \right) \left( \frac{\mathcal{N}_{\text{h,seed}}}{10^{-4} \text{ cMpc}^{-3}} \right). \quad (36)$$

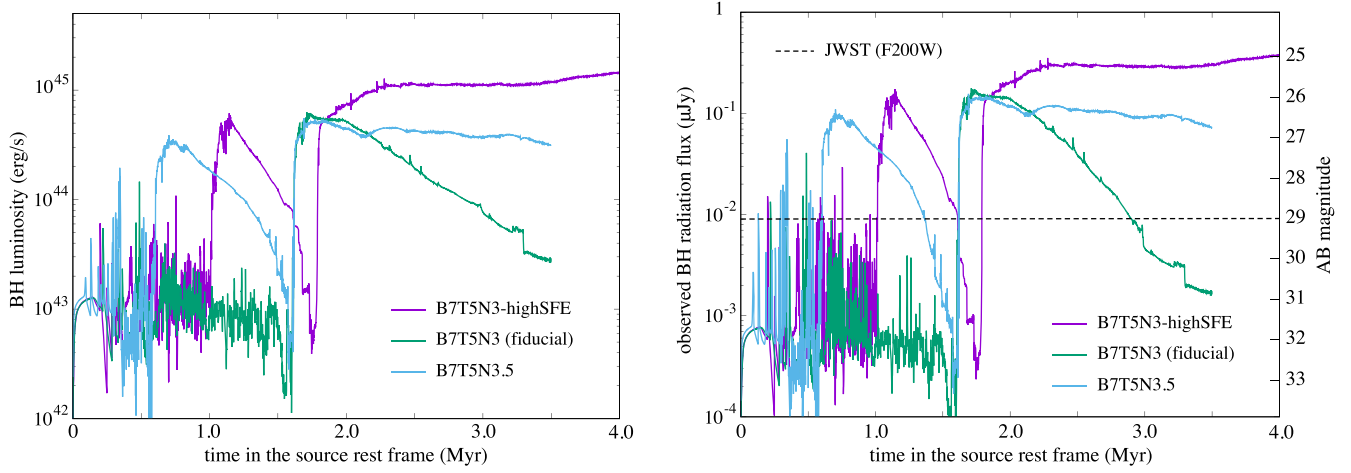


**Figure 9.** Left panel: radiative luminosity produced from a rapidly accreting BH for the high-SFE case (purple), the fiducial case (green), and the high-density case with  $n_c = 10^{3.5} \text{ cm}^{-3}$  (cyan). During the growing phases from  $M_* = 10^5 M_\odot$  to  $\sim 10^6 M_\odot$ , the luminosities becomes as high as  $L_* \simeq (0.3 - 1.2) \times 10^{45} \text{ erg s}^{-1}$ . Right panel: observed radiative flux at  $\lambda_{\text{obs}} = 1.98 \mu\text{m}$  emitted from an accreting BH in a protogalaxy at  $z = 15$  predicted for the three models. The viewing angle is set to  $\theta_{\text{obs}} = 30^\circ$ . The horizontal, dashed line shows the signal-to-noise ratio (S/N) = 10 detection limit of JWST/NIRCam imaging with the F200W filter in a 10 ks exposure time.

We note that if the limiting magnitude is  $m_{\text{AB}} < 27$  mag, the observable duration becomes shorter, and the number of detections is lowered.

The detailed modeling of their SED and the multiband selection and spectroscopic diagnosis of accreting seed BH candidates will be discussed in future work. Note that some previous studies modeled the radiation spectrum of an accreting seed BH using a spherically symmetric one-dimensional flow structure (Pacucci et al. 2015; Natarajan et al. 2017; Valiante et al. 2018).

#### 4. Analytical Derivation of the Conditions for Rapid Accretion

We here derive the conditions required for the onset of rapid mass accretion onto a seed BH embedded within bulge stars. Based on the RHD simulation results, the transition is triggered when (1) the I-front is confined within the core region without propagating outward and (2) a sufficient amount of neutral gas is supplied from larger radii without being suppressed by radiative feedback. In what follows, we quantify the two conditions with analytical expressions.

Let us consider that an accreting BH emits ionizing radiation at a rate of  $Q_0$  and the radiation propagates outward within a gas cloud with a distribution given by Equation (29). As a reference value, we estimate the size of the I-front in a uniform density with  $n_c$  as

$$r_{\text{ion}} = \left( \frac{3Q_0}{4\pi\alpha_{\text{rec,B}}n_c^2} \right)^{1/3}, \quad (37)$$

$$\simeq 25.5 \lambda^{1/3} M_5^{1/3} n_{c,3}^{-2/3} \left( \frac{T_{\text{HII}}}{7 \times 10^4 \text{ K}} \right)^{0.28} \text{ pc}$$

where  $\alpha_{\text{rec,B}}$  is the case-B radiative recombination rate coefficient,  $T_{\text{HII}}$  is the temperature of the ionized gas, the number flux of ionizing photons is given by  $Q_0 \simeq 0.173 L_*/(h\nu_{\text{Ly}})$  for the radiation spectral model (Equation (22)), and  $\lambda (\equiv L_*/L_{\text{Edd}})$  is the Eddington ratio. However, this estimate in Equation (37) is no longer valid when the I-front size reaches the radius where the density distribution decreases steeply. With the gas remaining at

rest, the critical power-law index of the density profile ( $\rho \propto r^{-\beta}$ ) for continuous expansion of the I-front is given by  $\beta = 3/2$  (Franco et al. 1990). Therefore, for the given initial density profile, one defines the critical radius, outside which the power-law index is steeper than the critical value and the I-front expansion is accelerated, by  $r_{\text{crit}} = \sqrt{3} r_0$  or

$$r_{\text{crit}} = 27.4 T_{\text{vir},5}^{1/2} n_{c,3}^{-1/2} \text{ pc}. \quad (38)$$

Thus, the first condition for the transition is given by  $r_{\text{crit}} \gtrsim r_{\text{ion}}$  or

$$M_* \lesssim 2 \times 10^5 T_{\text{vir},5}^{3/2} n_{c,3}^{1/2} \left( \frac{\lambda}{0.5} \right)^{-1} M_\odot, \quad (39)$$

where the Eddington ratio is set to  $\lambda = 0.5$ , which is the typical value before the transition to rapid mass accretion.

Next, we consider the condition where radiative feedback does not affect mass inflows from larger radii. Namely, this requires the effective gravitational influence radius to be larger than the size of the ionized region, i.e.,  $r_{\text{inf}} \gtrsim r_{\text{ion}}$ . The effective gravitational influence radius is calculated with the balance between the total (BH+bulge+DM) gravitational force and the gas-pressure gradient force as

$$\alpha \frac{c_s^2}{r} \simeq \frac{GM_*}{r^2} + \frac{GM_{\text{bulge}}}{(r + r_c)^2} - \frac{2k_B T_{\text{vir}} f(c_N)}{\mu m_p r_s} g(x) \quad (40)$$

where  $x = r/r_s$ ,  $f(c_N) \simeq 5$  at  $1 \lesssim c_N \lesssim 5$ , and  $g(x) = [x - (1+x)\ln(1+x)]/[x^2(1+x)]$ . In the cases of interest, where  $r_{\text{ion}} \lesssim r_{\text{crit}} \ll r_s$ , the third term on the right-hand side can be approximated as  $\approx 5xk_B T_{\text{vir}}/(\mu m_p)$ , and the first term is negligible compared to the second term. Therefore, the force balance at  $r_{\text{crit}} \lesssim r \ll r_s$ , where  $\alpha \simeq 2$ , is governed by the equation of

$$2c_s^2 \simeq \frac{GM_* r}{(r + r_c)^2} + \frac{5k_B T_{\text{vir}}}{\mu m_p} \left( \frac{r}{r_s} \right). \quad (41)$$



In addition, when  $M_* \ll 1.7 \times 10^8 T_{\text{vir},5} n_{\text{c},3}^{-1} M_\odot$ , the bulge size is sufficiently small ( $r \gg r_c$ ), and the gravitational influence radius is expressed by<sup>12</sup>

$$r_{\text{inf}} \simeq \frac{GM_*}{2c_s^2}. \quad (42)$$

Note that Equation (42) is identical to the bulge-gravitational influence radius that approximates the bulge to be a point gravitational source. Therefore, the condition of  $r_{\text{inf}} \gtrsim r_{\text{ion}}$  is rewritten as

$$\frac{M_*}{M_\bullet} \gtrsim 82 M_5^{-2/3} n_{\text{c},3}^{-2/3} \left( \frac{\lambda}{0.5} \right)^{1/3} \left( \frac{T_{\text{HII}}}{7 \times 10^4 \text{ K}} \right)^{1.28}, \quad (43)$$

where the sound speed is evaluated with the temperature in the ionized region as  $c_s \simeq 29.6 \text{ km s}^{-1} (T_{\text{HII}}/7 \times 10^4 \text{ K})^{1/2}$ . Indeed, for  $M_\bullet = 10^5 M_\odot$ , the transient super-Eddington accretion mode can be triggered when the bulge mass is as massive as  $M_* \gtrsim 10^7 M_\odot$  (our fiducial case). Finally, combining the two conditions given by Equations (39) and (43), we obtain the bulge–BH mass relation required to feed the BH efficiently as

$$\frac{M_*}{M_\bullet} \gtrsim 1.03 \times 10^2 \lambda n_{\text{c},3}^{-1} T_{\text{vir},5}^{-1}, \quad (44)$$

where the dependence on  $T_{\text{HII}}$  is omitted. For our cases with  $M_\bullet = 10^5 M_\odot$ , the critical bulge mass for the onset of rapid accretion is estimated from Equation (44) as  $M_* \simeq 10^7 M_\odot$ . This is consistent with the result of our parameter studies discussed in Section 3.2.2.

In summary, for two given quantities to characterize the properties of gas in a DM halo ( $T_{\text{vir}}$  and  $n_c$ ), we discuss whether seed BHs can grow via mass accretion at rates exceeding the Eddington value. This transient growing phase takes place when the ionizing radiation produced by the BH does not break the gaseous core (see Equation (39)) and a massive bulge with  $M_* \gtrsim 100 M_\bullet$  attracts a sufficient amount of gas within its gravitational influence radius (see Equation (44)).

Finally, we note that the critical bulge-to-BH mass ratio in Equation (44) is  $\sim 10$  times higher than that obtained in the previous study by Park et al. (2016), where the gravitational effect of bulge stars is considered in spherically symmetric one-dimensional RHD simulations for BH accretion. Compared to their work, we further take into account the multidimensional effect (e.g., gas angular momentum), irradiation by bulge stars, and metallicity and also adopt a different bulge model.<sup>13</sup> However, the difference in the critical mass ratio is mainly caused by the initial density distribution. Since Park et al. (2016) adopted a uniform density distribution as their initial conditions, the I-front always has a maximum size without continuous expansion. On the other hand, in our cases where the initial density profile consists of the core and envelope, it follows that  $n \propto r^{-2}$ . Therefore, the condition of Equation (39) has to be required to trigger rapid BH accretion. If we adopted a uniform density distribution, only the condition of Equation (43) would be considered. For  $M_* = 10^6 M_\odot$ , the

critical mass ratio estimated from Equation (43) is  $M_*/M_\bullet \simeq 18$ , which is consistent with that in Park et al. (2016).

## 5. Discussion

### 5.1. Feasible Conditions of Rapid BH Accretion in the Galaxy Assembly

In this section, we discuss whether seed BHs formed in high-redshift protogalaxies experience rapidly growing phases. Let us first consider a BH with  $M_\bullet = 10^5 M_\odot$ . From the condition of Equation (39), the host DM halo is required to be as massive as

$$M_h \gtrsim 2 \times 10^9 M_{*,5} n_{\text{c},3}^{-1/2} \left( \frac{1+z}{16} \right)^{-3/2} M_\odot, \quad (45)$$

or equivalently,  $T_{\text{vir}} \gtrsim 10^5 M_{*,5}^{2/3} n_{\text{c},3}^{-1/3} \text{ K}$ . Now, we define the ratio of the galaxy stellar mass to the DM halo mass as  $f_*$  ( $\equiv M_*/M_h$ ) and assume that the bulge mass in the protogalaxy is comparable to the total stellar mass. Then, using the condition of Equation (44), we obtain

$$f_* \gtrsim 5.2 \times 10^{-3} M_{*,5}^{-2/3} n_{\text{c},3}^{-1/6} \left( \frac{1+z}{16} \right)^{3/2}. \quad (46)$$

The required value of  $f_*$  corresponds to  $\gtrsim 3\%$  of the conversion efficiency from gas into stars (i.e., the SFE,  $\epsilon_*$ ), assuming the cosmic mean baryon fraction  $f_b = \Omega_b/\Omega_m \simeq 0.16$ . This value is consistent with those inferred by abundance matching and the observed UV luminosity function of galaxies at  $z \simeq 6$  (Bouwens et al. 2015). Moreover, this choice of  $\epsilon_* \sim 0.03$ – $0.05$  explains the cosmic reionization history without violating the optical depth of the universe to electron scattering measured by the Planck satellite (Visbal et al. 2015; Inayoshi et al. 2021).<sup>14</sup> We adopt a single value of  $\epsilon_* = 0.05$ ; therefore, the condition of Equation (46) is rewritten as

$$M_\bullet \gtrsim 5.2 \times 10^4 n_{\text{c},3}^{-1/4} \left( \frac{\epsilon_*}{0.05} \right)^{-3/2} \left( \frac{1+z}{16} \right)^{9/4} M_\odot, \quad (47)$$

which holds for  $M_\bullet = 10^5 M_\odot$  seed BHs at  $z < 20$ .

To see the feasibility of rapid BH accretion in the hierarchical structure formation paradigm, we consider two different assembly histories of DM halos. One is the evolution of the high-redshift quasar main progenitors, i.e., the most massive halos at each epoch among halos that end up in  $M_h = 10^{12} M_\odot$  at  $z = 6$ . In Figure 10, we present  $10^4$  merger trees of the high-redshift quasar main progenitors (gray curves), corresponding to the  $3\sigma$ – $4\sigma$  mass variance, and the median halo mass is shown by the dashed curve. Along with the merger history of the high-redshift quasar hosts, there is a parameter region where the two conditions given by Equations (45) and (47) are satisfied, and the seed BH can experience transient super-Eddington accretion phases (red curve). The other one is the assembly history of the typical first galaxies that form in DM halos with  $M_h \gtrsim 10^7 M_\odot$  at  $z \simeq 10$ , corresponding to the  $2\sigma$  mass variance (blue curve). Along with this evolutionary track, seed BHs with  $M_\bullet = 10^5 M_\odot$  could grow via rapid accretion at

<sup>12</sup> Another solution of  $r \gtrsim 0.4 (T_g/T_{\text{vir}}) r_s$  is not adopted.

<sup>13</sup> Park et al. (2016) modeled it so that the mean stellar density within  $r_c$  is consistent with that of the Milky Way. On the other hand, we model the bulge mass–size relation so that the observed  $M_*$ – $\sigma_e$  relation is reproduced (see Section 2), yielding a more concentrated bulge.

<sup>14</sup> An empirical model for linking galaxy SFRs to the properties of their host halos (UNIVERSEMACHINE; Behroozi et al. 2020) predicts the bulge-to-halo-mass ratio as  $f_* \sim 3 \times 10^{-4} (M_h/10^9 M_\odot)^{0.75}$  at  $10 < z < 15$  over  $10^9 \lesssim M_h/M_\odot \lesssim 10^{10}$ . The error size with 84% confidence is  $\sim \pm(0.3\text{--}0.5)$  dex at  $z \simeq 10$  and  $\sim \pm(0.7\text{--}1.0)$  dex at  $z \simeq 14$ , respectively. Indeed, the upper envelope of the predicted values at the halo mass range is consistent with  $f_* \sim 5 \times 10^{-3}$ .

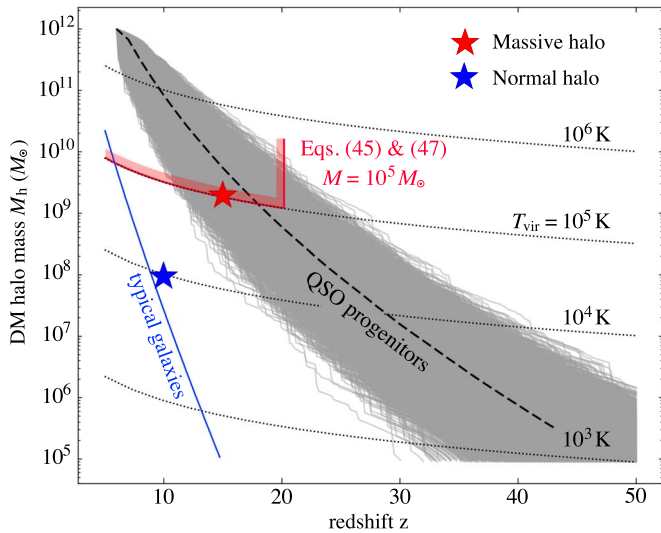


**Figure 10.** Summary of the analytical argument in Section 5.1 on the redshift-halo-mass plane. In the region enclosed with the two conditions of Equations (45) and (47), rapid mass accretion onto seed BHs with  $M_* = 10^5 M_\odot$  can take place (red curve). The star symbols represent the mass and redshift of the DM halos studied in this paper: massive halo (red) and normal halo (blue), respectively (see Table 1). The gray curves show  $10^4$  merger trees of the high-redshift quasar main progenitors, corresponding to the  $3\sigma$ – $4\sigma$  mass variance, and the black dashed curve represents the median halo mass. For comparison, the blue curve is the assembly history of the typical first galaxies, corresponding to the  $2\sigma$  mass variance. The dotted curves indicate constant virial temperatures, the values of which are denoted by numbers in the figure.

$z < 6$  (i.e.,  $T_{\text{vir}} \gtrsim 10^5$  K). It is also worth noting that strong suppression of BH growth from  $M_* \sim 10^5 M_\odot$  in typical galaxies with  $T_{\text{vir}} \simeq 10^4$  K is commonly seen in cosmological hydrodynamical simulations. For instance, Latif et al. (2018) showed that the early growth of a  $10^5 M_\odot$  BH is totally quenched in an atomic-cooling halo with  $2\sigma$  mass variance.

Next, we briefly discuss the cases with different BH masses. When the seed mass is  $M_* = 10^4 M_\odot$ , the halo condition yields  $T_{\text{vir}} \gtrsim 2 \times 10^4$  K, but the high value of  $f_*$  can be achieved at a lower redshift of  $1 + z \lesssim 7.8$  ( $\epsilon_*/0.05$ ) $^{2/3}$ . On the other hand, when the seed mass is  $M_* = 10^6 M_\odot$ , the halo condition is satisfied in massive DM halos with  $M_h \gtrsim 10^{11} M_\odot$  (or  $T_{\text{vir}} \gtrsim 4.6 \times 10^5$  K), where all of the high-redshift quasar progenitor halos are expected to have sufficiently massive bulges. However, the host galaxies formed in those massive halos would be already polluted by heavy elements. While our simulation results hold for lower-metallicity environments with  $Z \simeq 0.01 Z_\odot$ , the radiative feedback effect caused by the accreting BH would be stronger in more metal-enriched environments. This would quench their efficient growth of BHs and change the accretion mode to the Eddington-limited one. Exploration of the critical metallicity to terminate super-Eddington accretion and studying the impact of the cosmological metal-enrichment processes is left for future work.

### 5.2. Early Coevolution of Seed BHs with Host Galaxies

The empirical relation between the mass of SMBHs and the properties of their host galaxies is considered to be one of the most important outcomes caused by their coevolution over the cosmic timescale (e.g., Magorrian et al. 1998; Ferrarese & Merritt 2000; Kormendy & Ho 2013). Theoretical models for explaining the tight correlations have been proposed, but the origin is still unclear. To understand the nature of these

correlations, it is critically important to study them beyond the local universe, characterizing how and when the relations have been established and evolved until now. So far, a large number of observational studies have extensively investigated the redshift dependence of the BH-to-bulge mass ratio of  $M_*/M_*$  and overall suggested its positive redshift dependence, i.e., the ratio increases with redshift (Bennert et al. 2011; Schramm & Silverman 2013; Ding et al. 2020). Beyond  $z \sim 6$ , the Atacama Large Millimeter/submillimeter Array (ALMA) is a powerful tool to measure the dynamical mass of gas in quasar host galaxies and allows us to explore the early stage of the BH/galaxy correlation (e.g., Wang et al. 2010, 2013; Venemans et al. 2017). In addition, observations with the Subaru HSC provide low-luminosity and less-massive BH samples, which are unique populations to determine the  $M_*/M_*$  ratio at  $z > 6$  (Izumi et al. 2019, 2021). Figure 11 shows the distribution of  $z > 6$  quasars compiled in Izumi et al. (2021), together with those in the local universe (Kormendy & Ho 2013). First, the brightest  $z > 6$  quasars with  $M_{1450} < -25$  mag tend to have  $M_*/M_*$  ratios higher than those seen in the local universe. Namely, the mass ratio for those brightest objects is boosted by a factor of  $\sim 10$  (blue dashed line; Pensabene et al. 2020). On the other hand, the fainter quasars with  $M_{1450} > -25$  mag appear to follow the local relation, although those BHs are considered to grow at rates of  $\gtrsim 0.05$  SFR and will be overmassive at lower redshifts.<sup>15</sup> We note that for all of the  $z > 6$  samples, the values of the  $x$ -axis are not the bulge mass of their host galaxies but the dynamical mass measured by [C II]  $158 \mu\text{m}$  lines. In general, the dynamical mass is considered to be higher than the true bulge mass. With a high-resolution ALMA observation, Izumi et al. (2021) found that the gas dynamics of the core component of a low-luminosity quasar at  $z = 7.07$  (HSC J1243+0100) is governed by rotation associated with a compact bulge and estimated its mass as  $\sim 50\%$  of the [C II]-based dynamical mass. Therefore, the correlation at  $z > 6$  might be shifted to the left if the conversion factor from the dynamical mass to the bulge mass is taken into account.

At the left-bottom corner of Figure 11, we present the evolution tracks of the  $M_*/M_*$  ratio obtained from our simulations. When the bulge mass is  $M_* < 10^7 M_\odot$  (purple curve), the seed BH hardly grows in mass, owing to radiative feedback, and the  $M_*/M_*$  moves to the right, i.e., only the bulge mass grows. When the bulge is as massive as  $M_* \geq 10^7 M_\odot$  (magenta and red curves), the efficient mass accretion phases are triggered, and thus the BH mass abruptly increases within  $\sim$ a few megayears. As a result, the  $M_*/M_*$  ratio becomes as high as  $\sim 0.03$ – $0.05$ , which is consistent with those of  $z > 6$  (see also the line obtained by Pensabene et al. 2020). In the high-SEF model ( $\epsilon_* = 0.5$ ), where the bulge mass reaches  $M_* \simeq 3 \times 10^7 M_\odot$  within  $\sim 3$  Myr, the BH-to-bulge mass ratio is  $M_*/M_* \simeq 0.03$  at the end of the simulation.<sup>16</sup> After the

<sup>15</sup> In this paper, overmassive BHs are referred to as a BH population with a BH-to-galaxy mass ratio higher than that observed in the local universe;  $M_*/M_* \gtrsim 4.9^{+0.5}_{-0.3} \times 10^{-3}$  (Kormendy & Ho 2013). We employ this terminology to clearly contrast the difference between the overmassive and undermassive BH population with respect to the local value (see Figure 11). Note that a previous study by Agarwal et al. (2013) used a term of “obese BH,” which refers to a BH population dominating over the stellar mass of its host galaxy at least in the initial growing stage (i.e.,  $M_*/M_* > 1$ ).

<sup>16</sup> A semi-analytical study by Agarwal et al. (2013) proposed a pathway yielding a more extreme BH-to-galaxy mass ratio of  $M_*/M_* > 1$  in atomic-cooling halos with  $T_{\text{vir}} \simeq 10^4$  K. Based on their model, the number density of such obese BHs with  $M_* > 10^7 M_\odot$  is estimated as  $\sim 0.03 \text{ cMpc}^{-3}$  at  $z \sim 6$ . However, the cumulative mass density of those BHs overshoots the local mass density of SMBHs (e.g., Shankar et al. 2009) and a constraint from the unresolved cosmic X-ray background (e.g., Salvaterra et al. 2012).

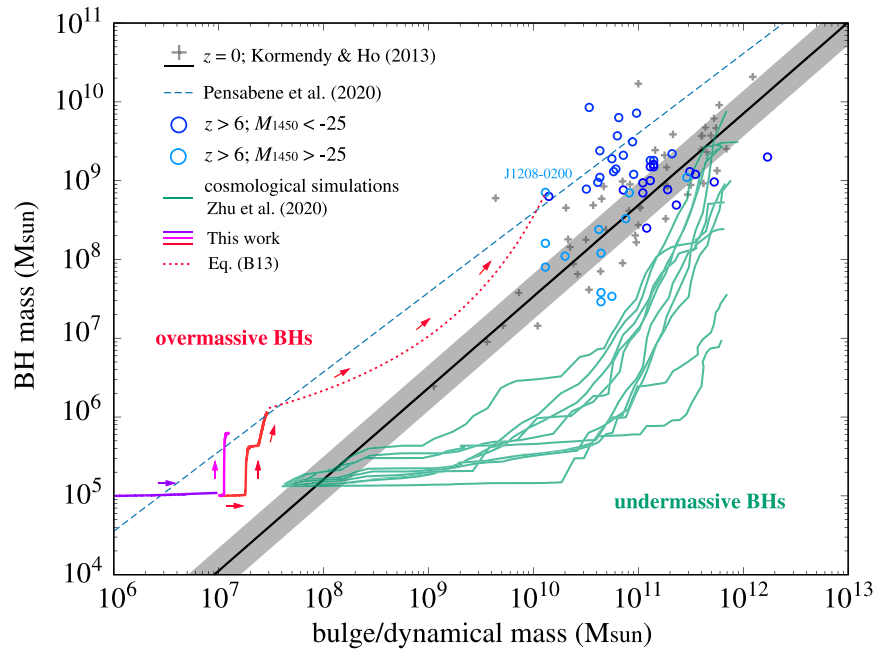


**Figure 11.** The  $M_{\bullet}$ – $M_{\star}$  relation for the three simulations: B7T5N3-highSFE (red), B7T5N3 (magenta), and B6T5N3 (purple). Circle symbols show the  $z > 6$  quasar samples compiled by Izumi et al. (2019, 2021): brighter ones with  $M_{1450} < -25$  (blue) and fainter ones with  $M_{1450} > -25$  (cyan). The cross symbols are the observational samples in the local universe provided by Kormendy & Ho (2013). Each line represents the local relation of  $M_{\bullet}/M_{\star}$  (black solid, with  $\sim 1\sigma$  errors), and the best-fit relations for the brightest  $z > 6$  quasars by Pensabene et al. (2020). The red dotted curve presents the evolutionary track of the  $M_{\bullet}/M_{\star}$  ratio after rapid accretion phases predicted by a phenomenological model (see Appendix B). As a reference, the evolutionary tracks of the  $M_{\bullet}/M_{\star}$  ratio obtained by cosmological simulations (Zhu et al. 2020) are overlaid (green curves).

rapid BH growing phase terminates, both the BH and host galaxy evolve in mass and reach the observed values as high-redshift quasars. As an example, we present the subsequent BH/galaxy evolutionary track to a  $z > 6$  HSC quasar (Izumi et al. 2019) predicted by a phenomenological model (see more details in Appendix B). In summary, seed BHs formed in high-redshift quasar hosts can be substantially overmassive during the early bulge assembly at  $z \gtrsim 15$ , and the mass ratio would approach the ratio of  $M_{\bullet}/M_{\star}$  seen at  $z \sim 6$  via the subsequent growth.

It is worth noting that most cosmological simulations studying the BH-galaxy coevolution concluded that seed BHs hardly grow in mass via gas accretion because dense, cold gas is expelled by energetic SN feedback associated with star formation (e.g., Sijacki et al. 2009; Habouzit et al. 2017; Lupi et al. 2019). As a result of SN feedback, BH growth is strongly quenched until the host galaxies become heavier than  $M_{\star} \gtrsim 10^9 M_{\odot}$ , whose critical stellar mass depends on the sub-grid models for star formation, SN feedback, and AGN feedback. There is a model parameter set for which the most massive BHs in their simulations can reach  $M_{\bullet} \simeq 10^9 M_{\odot}$  by  $z \sim 6$ . However, the predicted shape of the  $M_{\bullet}$ – $M_{\star}$  relation shows that most of the BHs are *undermassive*, compared to the local relation (e.g., Zhu et al. 2020; Valentini et al. 2021). As a reference, the evolutionary tracks of the  $M_{\bullet}/M_{\star}$  ratio obtained by Zhu et al. (2020)<sup>17</sup> are overlaid in Figure 11 (green curves).

As discussed in Inayoshi et al. (2020), there are important limitations of current numerical simulations. First, most large-scale cosmological simulations resolve the dynamics of

DM/gas/stars on galactic scales at  $\sim O(\text{kpc})$ , but they do not resolve the BH gravitational influence radius. Second, owing to simplified star formation models where gas particles denser than a threshold are replaced with stars, dense clouds in the nuclear region would be disrupted, and thus the BH growth could be quenched as seen in many cosmological simulation studies. In contrast, as shown in our simulations that resolve sub-parsec scales, a fraction of seed BHs that were born in highly biased regions of the universe with mass variance of  $\gtrsim 3\sigma$ – $4\sigma$  could be fed through dense, cold accretion flows (see also Li et al. 2021b). Additionally, the existence of such *overmassive* BHs in protogalaxies will provide us with a unique opportunity to detect highly accreting seed BHs in the very early universe at  $z > 10$ , unlike the undermassive BH scenarios supported by cosmological simulations.

### 5.3. Young Quasars with Low Radiative Efficiencies

Our RHD simulations suggest the existence of high-redshift quasars that accrete at super-Eddington rates and fade out on a timescale of  $\sim$ a few megayears. The duration of such rapid accretion is generally consistent with lifetimes of  $z \gtrsim 6$  quasars ( $t_Q \lesssim 1$ – $10$  Myr), which are estimated by the measurement of the physical extents of hydrogen Ly $\alpha$  proximity zones observed in the rest-frame UV spectra (e.g., Eilers et al. 2018; Davies et al. 2019; Eilers et al. 2021). Since the inferred quasar lifetimes are substantially shorter than the  $e$ -folding timescale assuming Eddington-limited accretion,  $t_{\text{Edd}} (\equiv M_{\bullet}/\dot{M}_{\text{Edd}}) \simeq 45$  Myr, some of those  $z \gtrsim 6$  quasars are expected to undergo radiatively inefficient super-Eddington accretion to grow up to  $M_{\bullet} \sim 10^9 M_{\odot}$  in such a short duration. For instance, Davies et al. (2019) proposed that two  $z > 7$  quasars (ULAS J1120+0641 and ULAS J1342+0928) would have a small radiative efficiency significantly below  $\eta_0 \simeq 0.1$ .

<sup>17</sup> Zhu et al. (2020) have extensively investigated the effect of feedback, BH seeding, and accretion models on the BH growth. Among their simulation results, we show the cases where the initial BH mass is  $M_{\bullet} = 10^5 M_{\odot}$  for comparison.



Based on the above, multiple episodes of rapid accretion would be an intriguing counterpart of such young high-redshift quasars; although, the observed quasars are hosted in substantially heavier halos and exhibit SFRs higher than we consider. Moreover, the episodic nature of quasar activity produces a complex structure of ionized and neutral gas surrounding the growing BH, unlike the situation where continuous output of radiation from the BH is assumed (the so-called “light-bulb” light-curve model). The variable light-curve effect on the formation of proximity zones needs to be explored in more detail (see, e.g., Davies et al. 2020). Performing RT calculations of Ly $\alpha$  lines under a realistic density profile obtained from simulations for BH accretion is left for future investigations.

## 6. Summary

We study the early growth of massive seed BHs via accretion at the centers of protogalaxies where the stellar bulge component is assembled, performing axisymmetric two-dimensional RHD simulations. We find that when a seed BH with  $M_{\bullet} \sim 10^5 M_{\odot}$  is embedded in dense metal-poor gas ( $Z = 0.01 Z_{\odot}$ ) with a density of  $n_{\text{c}} \gtrsim 100 \text{ cm}^{-3}$  and bulge stars with a total mass of  $M_{\star} \gtrsim 100 M_{\odot}$ , a massive gaseous disk feeds the BH efficiently at super-Eddington rates of  $\gtrsim 0.3\text{--}1 M_{\odot} \text{ yr}^{-1}$ . The peak rate of  $\dot{M}_{\bullet} \sim 10 M_{\odot} \text{ yr}^{-1}$  corresponds to  $\sim 2.5 \times 10^3 \dot{M}_{\text{Edd}}$ . This rapid accretion phase lasts until a good fraction of the gas bounded within the bulge accretes onto the BH, although the feeding rate is regulated owing to strong outflows driven by ionizing radiation emitted from the accreting BH. As a result, the BH mass increases to  $\sim 10^6 M_{\odot}$  within  $\sim 2 \text{ Myr}$  after the onset of accretion bursts. In contrast, when the seed BH is surrounded by diffuse gaseous media and/or less-massive bulges, the BH accretion proceeds episodically due to radiative feedback, and thus the average accretion rate is limited below the Eddington rate.

We provide the analytical expressions of the conditions required for the onset of super-Eddington accreting phases of seed BHs embedded within growing bulge stars. This transient growing phase takes place when (1) the ionizing radiation produced by the BH does not break the gaseous core (see Equation (39)) and (2) a massive bulge with  $M_{\star} \gtrsim 100 M_{\odot}$  attracts a sufficient amount of gas within its gravitational influence radius (see Equation (44)). In the framework of the cosmological hierarchical structure formation, those conditions can be achieved for seed BHs formed in massive DM halos with masses of  $\gtrsim 10^9 M_{\odot}$  at  $z \sim 15\text{--}20$  (the virial temperature is  $T_{\text{vir}} \simeq 10^5 \text{ K}$ ). The host halos are heavier and rarer than those of typical first galaxies with  $T_{\text{vir}} \simeq 10^4 \text{ K}$ , but are more likely to end up in quasar hosts by  $z \simeq 6$ .

The rapid accretion mechanism found with our simulations that resolve sub-parsec scales naturally yields a high BH-to-bulge mass ratio of  $M_{\bullet}/M_{\star} \simeq 0.03\text{--}0.05$ . The ratio is significantly higher than that seen in the local universe, but is consistent with those of the brightest high-redshift quasars with  $M_{1450} < -25 \text{ mag}$ . The rarity of those overmassive BHs in the brightest quasars can also be explained by the fact that the transient rapid growth would take place in highly biased regions of the universe with mass variance of  $3\sigma\text{--}4\sigma$ . In contrast, most large-scale cosmological simulations that resolve the dynamics of DM/gas/stars on galactic scales at  $\sim O(\text{kpc})$  predict that SMBHs (or their seeds) tend to be undermassive at high redshifts compared to the local BH-galaxy correlation. Both observational and numerical studies are further required

to better understand the early development of the BH-galaxy correlation.

Moreover, the existence of such overmassive BHs provides us with a unique opportunity to detect highly accreting seed BHs with the upcoming observations by JWST. In fact, seed BHs accreting at super-Eddington rates produce radiative luminosities of  $L_{\bullet} \simeq (0.3\text{--}1.2) \times 10^{45} \text{ ergs}^{-1}$ , corresponding to  $L_{\bullet}/L_{\text{Edd}} \sim 4\text{--}16$ . If those BHs are in  $z \simeq 15$  protogalaxies, the radiation flux at  $\lambda_{\text{obs}} \simeq 2 \mu\text{m}$  ( $h\nu = 10 \text{ eV}$  in the rest frame) is estimated as  $\sim 0.01\text{--}0.2 \mu\text{Jy}$ , which corresponds to  $m_{\text{AB}} = 26\text{--}29 \text{ mag}$  and can be detectable with the  $S/N = 10$  detection limit of JWST NIRCcam imaging with the F200W filter in a 10 ks exposure time. If  $\gtrsim 4\%$  of the DM halos where the transition conditions are satisfied contain seed BHs, we are able to detect one rapidly accreting seed BH by JWST in its 10 fields of view.

We greatly thank Luis C. Ho, Takuma Izumi, and Mingyang Zhuang for constructive discussions. K.I. acknowledges support from the National Natural Science Foundation of China (12073003, 12003003, 11721303, 11991052, 11950410493), the National Key R&D Program of China (2016YFA0400702), and the China Manned Space Project with NO. CMS-CSST-2021-A06. R.N. is supported by the Special Postdoctoral Researcher (SPDR) Program at RIKEN and by a Grant-in-Aid for Research Activity Start-up (19K23469). T.H. acknowledges support from the JSPS KAKENHI grant Nos. 17H06360, 17H01102, and 19H01934. R.K. acknowledges financial support via the Emmy Noether and Heisenberg Research Grants funded by the German Research Foundation (DFG) under grant No. KU 2849/3 and 2849/9. R.K. also acknowledges financial support via the JSPS Invitational Fellowship for Research in Japan under the Fellowship ID S20156. The numerical simulations were performed with the Cray XC50 at the Center for Computational Astrophysics (CfCA) of the National Astronomical Observatory of Japan and with the High-performance Computing Platform of Peking University.

## Appendix A

### Bulge Size–Mass Relation and Formation

We consider the gravitational effect of bulge stars on the thermal dynamics of gas. In our simulations, we adopt a Hernquist density profile (Hernquist 1990)

$$\rho(r) = \frac{M_{\star}}{2\pi} \frac{r_{\text{c}}}{r(r + r_{\text{c}})^3}, \quad (\text{A1})$$

where  $M_{\star}$  is the total bulge mass, and  $r_{\text{c}}$  is the core radius. Integrating the density profile, the enclosed mass is given by

$$M(r) = M_{\star} \frac{r^2}{(r + r_{\text{c}})^2}, \quad (\text{A2})$$

and thus the half-mass-radius is calculated by

$$R_{\text{e}} = (1 + \sqrt{2})r_{\text{c}}. \quad (\text{A3})$$

Assuming isotropic motion of stars, the velocity dispersion is analytically calculated as

$$\sigma^2(r) = \frac{GM_{\star}}{r_{\text{c}}} \left[ xy^3 \ln\left(\frac{y}{x}\right) - \frac{x}{y} \left( \frac{1}{4} + \frac{y}{3} + \frac{y^2}{2} + y^3 \right) \right], \quad (\text{A4})$$

where  $x = r/r_c$  and  $y = 1 + x$ . The velocity dispersion at the half-mass-radius is

$$\sigma_e^2 \simeq 0.055 \frac{GM_\star}{r_c}. \quad (\text{A5})$$

In our paper, we quantify the core radius of  $r_c$  so that the correlation between  $M_\star$  and  $\sigma$  becomes consistent with that observed in the local universe (Kormendy & Ho 2013), as shown in Equation (9).

As described in Section 2.5, mass growth of the bulge is calculated with the SFR given by the DM halo properties (see Equation (32)) and the spherical mass distribution is imposed without solving stellar dynamics. Here, we briefly discuss the dynamical evolution of newly forming stars and show that a quasi-spherical stellar distribution can be achieved on a short timescale of  $\sim 0.1$  Myr. Let us consider an extreme case where star formation is suppressed by anisotropic irradiation by an accreting BH, but stars form in the equatorial region owing to the shadow effect. In this case, most of the stars are initially aligned with the disk plane. The relaxation timescale of the inclination is estimated as (Stewart & Ida 2000; Kocsis & Tremaine 2011)

$$t_{\text{relax,disk}} \simeq \frac{0.44\pi \langle e^2 \rangle^2 M_\star^2}{\Omega \langle m_\star \rangle M_\star \ln \Lambda} \simeq \frac{7.8 \times 10^4 \text{ yr}}{(\ln \Lambda / 7)} \times \left( \frac{r}{10 \text{ pc}} \right)^{3/2} \left( \frac{M_\star}{10^5 M_\odot} \right)^2 \left( \frac{M_\star}{10^7 M_\odot} \right)^{-3/2} \left( \frac{\langle m_\star \rangle}{3 M_\odot} \right)^{-1}, \quad (\text{A6})$$

where  $\langle e^2 \rangle^{1/2} = 0.3$  is the mean eccentricity,  $\langle m_\star \rangle$  is the mean stellar mass for the Salpeter IMF at  $1\text{--}100 M_\odot$ ,  $\Omega^{-1} = \sqrt{GM(<r)/r^3}$ , and  $\Lambda = \langle e^2 \rangle^{3/2} M_\star / \langle m_\star \rangle$ . Therefore, the disk stars will evolve into a quasi-spherical stellar cluster within  $\lesssim 0.1$  Myr, which is substantially shorter than the timescale of interest in our simulations. Note that this argument leads to a consistent result for stellar cluster formation around a massive heavy seed BH in an atomic-cooling halo (e.g., Kashiya & Inayoshi 2016).

## Appendix B

### Phenomenological Model for the $M_\bullet/M_\star$ Ratio

We provide a phenomenological model for calculating the redshift-dependent  $M_\bullet/M_\star$  ratio. First, we characterize the mass growth of a BH using an exponential function of time  $t$ ,

$$\frac{M_\bullet}{M_{\bullet i}} = \exp \left[ \langle A \rangle \frac{t - t_i}{t_{\text{Edd}}} \right], \quad (\text{B1})$$

where  $t_{\text{Edd}} = 45$  Myr is the Salpeter timescale,  $M_{\bullet i}$  is the BH mass at  $t = t_i$ ,  $A$  is the product of the Eddington ratio and duty cycle of the BH active phase, and  $\langle \cdot \rangle$  means the time-averaged value over the cosmic time duration of interest. Next, we express the mass growth of the host galaxy with a functional form of  $M_\star \propto e^{-Bz}$ , which is well known to nicely reproduce the mass growth of DM halos  $M_h$  (e.g., Wechsler et al. 2002; Neistein & Dekel 2008; Fakhouri et al. 2010). In fact, this redshift dependence leads to a halo-mass growth rate of  $d(\ln M_h)/dt \propto (1+z)^{5/2}$ , which has been understood based on the extended Press-Schechter formalism and also derived by

a fit to merger trees from cosmological  $N$ -body simulations (Dekel et al. 2013). Despite the complex nature of galaxy formation processes, cosmological hydrodynamical simulations have shown that the galaxy mass assembly history appears to follow a similar function form (e.g., see Figure 7 in Zhu et al. 2020). Note that the value of  $B$  for galaxy assembly is different from that of halo assembly. Motivated by this fact, we express the mass growth of the host galaxy as

$$\frac{M_\star}{M_{\star i}} = \exp \left[ \langle B \rangle \left( 1 - \frac{1+z}{1+z_i} \right) \right], \quad (\text{B2})$$

where  $M_{\star i}$  is the galaxy mass at  $z = z_i$ , and  $\langle B \rangle$  is a parameter to characterize the growth speed of the galaxy. Combining the two equations, we calculate the mass ratio of  $M_\bullet/M_\star$  as

$$\begin{aligned} \frac{M_\bullet}{M_\star} &= \frac{M_{\bullet i}}{M_{\star i}} \exp \left[ \langle A \rangle \frac{t - t_i}{t_{\text{Edd}}} - \langle B \rangle \left( 1 - \frac{1+z}{1+z_i} \right) \right], \\ &\simeq \frac{M_{\bullet i}}{M_{\star i}} \exp \left[ \langle A \rangle (D^{3/2} - 1) \frac{t_i}{t_{\text{Edd}}} - \langle B \rangle (1 - D^{-1}) \right], \end{aligned} \quad (\text{B3})$$

where  $D(z) \equiv (1+z_i)/(1+z)$  and  $t_H(z_i) = (2/3H_0) [\Omega_m(1+z_i)^3]^{-1/2}$  is the Hubble time at  $z = z_i$ , which is a good approximation in the matter dominant universe ( $z > 1$ ). Finally, we determine  $\langle A \rangle$  and  $\langle B \rangle$  by

$$\langle A \rangle = \frac{t_{\text{Edd}} \ln(M_{\bullet f}/M_{\bullet i})}{t_i D_f^{3/2} - 1} \quad \text{and} \quad \langle B \rangle = \frac{\ln(M_{\star f}/M_{\star i})}{1 - D_f^{-1}}, \quad (\text{B4})$$

where  $M_{\bullet f}$  and  $M_{\star f}$  are the BH and galaxy mass at  $z = z_f$  and  $D_f = D(z_f)$ , respectively.

As an example, we adopt a high-redshift HSC quasar (J1208-0200). For this quasar, the BH mass, dynamical mass, and redshift are measured as  $M_\bullet = 7.1 \times 10^8 M_\odot$ ,  $M_{\text{dyn}} = 1.3 \times 10^{10} M_\odot$ , and  $z = 6.2$ , respectively (Izumi et al. 2019). For simplicity, the galaxy mass is assumed to be equal to the dynamical mass (i.e.,  $M_\star = M_{\text{dyn}}$ ). Let us consider the BH after the transient rapid accretion phases ( $M_{\bullet i} = 1.3 \times 10^6 M_\odot$ ,  $M_{\star i} = 3 \times 10^7 M_\odot$ , and  $z_i = 15$ ) to be its seed (see the red curve in Figure 11). Following the method above, one obtains  $\langle A \rangle = 0.4765$  and  $\langle B \rangle = 11.039$ . The evolutionary track of the  $M_\bullet/M_\star$  ratio is shown in Figure 11 (red dashed curve). The mass ratio decreases initially, reaches a minimum value of  $\sim 0.01$  at  $z \simeq 10$ , and increases to the observed value.

## ORCID iDs

Kohei Inayoshi  <https://orcid.org/0000-0001-9840-4959>  
 Riouhei Nakatani  <https://orcid.org/0000-0002-1803-0203>  
 Daisuke Toyouchi  <https://orcid.org/0000-0003-3467-6079>  
 Takashi Hosokawa  <https://orcid.org/0000-0003-3127-5982>  
 Rolf Kuiper  <https://orcid.org/0000-0003-2309-8963>  
 Masafusa Onoue  <https://orcid.org/0000-0003-2984-6803>

## References

- Abel, T., Bryan, G. L., & Norman, M. L. 2002, *Sci*, **295**, 93
- Abramowicz, M. A., Czerny, B., Lasota, J. P., & Szuszkiewicz, E. 1988, *ApJ*, **332**, 646
- Agarwal, B., Davis, A. J., Khochfar, S., Natarajan, P., & Dunlop, J. S. 2013, *MNRAS*, **432**, 3438
- Akeson, R., Armus, L., Bachelet, E., et al. 2019, arXiv:1902.05569

- Alexander, T., & Natarajan, P. 2014, *Sci*, **345**, 1330
- Anglés-Alcázar, D., Faucher-Giguère, C.-A., Quataert, E., et al. 2017, *MNRAS*, **472**, L109
- Bai, X.-N. 2011, *ApJ*, **739**, 50
- Balbus, S. A., & Hawley, J. F. 1998, *RvMP*, **70**, 1
- Bañados, E., Venemans, B. P., Mazzucchelli, C., et al. 2018, *Natur*, **553**, 473
- Becerra, F., Greif, T. H., Springel, V., & Hernquist, L. E. 2015, *MNRAS*, **446**, 2380
- Behroozi, P., Conroy, C., Wechsler, R. H., et al. 2020, *MNRAS*, **499**, 5702
- Bennert, V. N., Auger, M. W., Treu, T., Woo, J.-H., & Malkan, M. A. 2011, *ApJ*, **742**, 107
- Bouwens, R. J., Illingworth, G. D., Oesch, P. A., et al. 2015, *ApJ*, **803**, 34
- Bromm, V., & Loeb, A. 2003, *ApJ*, **596**, 34
- Bromm, V., & Yoshida, N. 2011, *ARA&A*, **49**, 373
- Bullock, J. S., Kolatt, T. S., Sigad, Y., et al. 2001, *MNRAS*, **321**, 559
- Chon, S., Hosokawa, T., & Yoshida, N. 2018, *MNRAS*, **475**, 4104
- Chon, S., & Omukai, K. 2020, *MNRAS*, **494**, 2851
- Ciotti, L., & Ostriker, J. P. 2001, *ApJ*, **551**, 131
- Davies, F. B., Hennawi, J. F., & Eilers, A.-C. 2019, *ApJL*, **884**, L19
- Davies, F. B., Hennawi, J. F., & Eilers, A.-C. 2020, *MNRAS*, **493**, 1330
- Dekel, A., & Birnboim, Y. 2006, *MNRAS*, **368**, 2
- Dekel, A., Zolotov, A., Tweed, D., et al. 2013, *MNRAS*, **435**, 999
- Devecchi, B., & Volonteri, M. 2009, *ApJ*, **694**, 302
- Di Matteo, T., Khandai, N., DeGraf, C., et al. 2012, *ApJL*, **745**, L29
- Ding, X., Silverman, J., Treu, T., et al. 2020, *ApJ*, **888**, 37
- Draine, B. T., & Lee, H. M. 1984, *ApJ*, **285**, 89
- Dubois, Y., Pichon, C., Devriendt, J., et al. 2013, *MNRAS*, **428**, 2885
- Eilers, A.-C., Hennawi, J. F., & Davies, F. B. 2018, *ApJ*, **867**, 30
- Eilers, A.-C., Hennawi, J. F., Davies, F. B., & Simcoe, R. A. 2021, *ApJ*, **917**, 38
- Fakhouri, O., Ma, C.-P., & Boylan-Kolchin, M. 2010, *MNRAS*, **406**, 2267
- Fan, X. 2006, *NewAR*, **50**, 665
- Fernández, R., & Metzger, B. D. 2013, *ApJ*, **763**, 108
- Ferrarese, L., & Merritt, D. 2000, *ApJL*, **539**, L9
- Franco, J., Tenorio-Tagle, G., & Bodenheimer, P. 1990, *ApJ*, **349**, 126
- Fukushima, H., & Yajima, H. 2021, *MNRAS*, **506**, 5512
- Fukushima, H., Yajima, H., Sugimura, K., et al. 2020, *MNRAS*, **497**, 3830
- Galli, D., & Palla, F. 1998, *A&A*, **335**, 403
- Glover, S. C. O., & Jappsen, A.-K. 2007, *ApJ*, **666**, 1
- Grimm, H.-J., Gilfanov, M., & Sunyaev, R. 2003, *MNRAS*, **339**, 793
- Habouzit, M., Volonteri, M., & Dubois, Y. 2017, *MNRAS*, **468**, 3935
- Haiman, Z. 2013, in *The First Galaxies, Astrophysics and Space Science Library*, ed. T. Wiklund, B. Mobasher, & V. Bromm, Vol. 396 (Berlin: Springer), 293
- Hernquist, L. 1990, *ApJ*, **356**, 359
- Hirano, S., Hosokawa, T., Yoshida, N., et al. 2014, *ApJ*, **781**, 60
- Hollenbach, D., & McKee, C. F. 1989, *ApJ*, **342**, 306
- Hosokawa, T., Omukai, K., Yoshida, N., & Yorke, H. W. 2011, *Sci*, **334**, 1250
- Iliev, I. T., & Shapiro, P. R. 2001, *MNRAS*, **325**, 468
- Inayoshi, K., Haiman, Z., & Ostriker, J. P. 2016, *MNRAS*, **459**, 3738
- Inayoshi, K., Ichikawa, K., Ostriker, J. P., & Kuiper, R. 2019, *MNRAS*, **486**, 5377
- Inayoshi, K., Kashiyama, K., Visbal, E., & Haiman, Z. 2021, *ApJ*, **919**, 41
- Inayoshi, K., & Omukai, K. 2011, *MNRAS*, **416**, 2748
- Inayoshi, K., Omukai, K., & Tasker, E. 2014, *MNRAS*, **445**, L109
- Inayoshi, K., & Tanaka, T. L. 2015, *MNRAS*, **450**, 4350
- Inayoshi, K., Visbal, E., & Haiman, Z. 2020, *ARA&A*, **58**, 27
- Inoue, A. K. 2011, *MNRAS*, **415**, 2920
- Izumi, T., Matsuoka, Y., Fujimoto, S., et al. 2021, *ApJ*, **914**, 36
- Izumi, T., Onoue, M., Matsuoka, Y., et al. 2019, *PASJ*, **71**, 111
- Jeon, M., Pawlik, A. H., Greif, T. H., et al. 2012, *ApJ*, **754**, 34
- Jiang, Y.-F., Stone, J. M., & Davis, S. W. 2014, *ApJ*, **796**, 106
- Johnson, J. L., Khochfar, S., Greif, T. H., & Durier, F. 2011, *MNRAS*, **410**, 919
- Kashiyama, K., & Inayoshi, K. 2016, *ApJ*, **826**, 80
- Kawinwanichakij, L., Silverman, J. D., Ding, X., et al. 2021, *ApJ*, **921**, 38
- Kitayama, T., & Yoshida, N. 2005, *ApJ*, **630**, 675
- Kitayama, T., Yoshida, N., Susa, H., & Umemura, M. 2004, *ApJ*, **613**, 631
- Kocsis, B., & Tremaine, S. 2011, *MNRAS*, **412**, 187
- Kormendy, J., & Ho, L. C. 2013, *ARA&A*, **51**, 511
- Kratter, K., & Lodato, G. 2016, *ARA&A*, **54**, 271
- Kuiper, R., Klahr, H., Beuther, H., & Henning, T. 2010, *ApJ*, **722**, 1556
- Kuiper, R., Klahr, H., Beuther, H., & Henning, T. 2011, *ApJ*, **732**, 20
- Kuiper, R., Yorke, H. W., & Mignone, A. 2020, *ApJS*, **250**, 13
- Latif, M. A., Schleicher, D. R. G., Schmidt, W., & Niemeyer, J. 2013, *MNRAS*, **433**, 1607
- Latif, M. A., Volonteri, M., & Wise, J. H. 2018, *MNRAS*, **476**, 5016
- Levermore, C. D., & Pomraning, G. C. 1981, *ApJ*, **248**, 321
- Li, J., Silverman, J. D., Ding, X., et al. 2021a, *ApJ*, **918**, 22
- Li, W., Inayoshi, K., & Qiu, Y. 2021b, *ApJ*, **917**, 60
- Li, Y., Hernquist, L., Robertson, B., et al. 2007, *ApJ*, **665**, 187
- Lodato, G., & Natarajan, P. 2006, *MNRAS*, **371**, 1813
- Lupi, A., Haiman, Z., & Volonteri, M. 2021, *MNRAS*, **503**, 5046
- Lupi, A., Volonteri, M., Decarli, R., et al. 2019, *MNRAS*, **488**, 4004
- Lusso, E., Worseck, G., Hennawi, J. F., et al. 2015, *MNRAS*, **449**, 4204
- Magorrian, J., Tremaine, S., Richstone, D., et al. 1998, *AJ*, **115**, 2285
- Matsuoka, Y., Onoue, M., Kashikawa, N., et al. 2016, *ApJ*, **828**, 26
- Matsuoka, Y., Strauss, M. A., Kashikawa, N., et al. 2018, *ApJ*, **869**, 150
- McKinney, J. C., Dai, L., & Avara, M. J. 2015, *MNRAS*, **454**, L6
- McKinney, J. C., & Gammie, C. F. 2004, *ApJ*, **611**, 977
- Mignone, A., Bodo, G., Massaglia, S., et al. 2007, *ApJS*, **170**, 228
- Milosavljević, M., Bromm, V., Couch, S. M., & Oh, S. P. 2009, *ApJ*, **698**, 766
- Mineo, S., Gilfanov, M., Lehmer, B. D., Morrison, G. E., & Sunyaev, R. 2014, *MNRAS*, **437**, 1698
- Mo, H. J., Mao, S., & White, S. D. M. 1998, *MNRAS*, **295**, 319
- Mortlock, D. J., Warren, S. J., Venemans, B. P., et al. 2011, *Natur*, **474**, 616
- Mowla, L., van der Wel, A., van Dokkum, P., & Miller, T. B. 2019, *ApJL*, **872**, L13
- Nakatani, R., Hosokawa, T., Yoshida, N., Nomura, H., & Kuiper, R. 2018a, *ApJ*, **857**, 57
- Nakatani, R., Hosokawa, T., Yoshida, N., Nomura, H., & Kuiper, R. 2018b, *ApJ*, **865**, 75
- Narayan, R., Sądowski, A., Penna, R. F., & Kulkarni, A. K. 2012, *MNRAS*, **426**, 3241
- Natarajan, P. 2021, *MNRAS*, **501**, 1413
- Natarajan, P., Pacucci, F., Ferrara, A., et al. 2017, *ApJ*, **838**, 117
- Navarro, J. F., Frenk, C. S., & White, S. D. M. 1997, *ApJ*, **490**, 493
- Neistein, E., & Dekel, A. 2008, *MNRAS*, **388**, 1792
- Ohsuga, K., Mori, M., Nakamoto, T., & Mineshige, S. 2005, *ApJ*, **628**, 368
- Omukai, K. 2001, *ApJ*, **546**, 635
- Omukai, K., & Nishi, R. 1998, *ApJ*, **508**, 141
- Onoue, M., Kashikawa, N., Matsuoka, Y., et al. 2019, *ApJ*, **880**, 77
- Pacucci, F., Ferrara, A., Volonteri, M., & Dubus, G. 2015, *MNRAS*, **454**, 3771
- Park, K., & Ricotti, M. 2011, *ApJ*, **739**, 2
- Park, K., & Ricotti, M. 2012, *ApJ*, **747**, 9
- Park, K., Ricotti, M., Di Matteo, T., & Reynolds, C. S. 2014, *MNRAS*, **437**, 2856
- Park, K., Ricotti, M., Natarajan, P., Bogdanović, T., & Wise, J. H. 2016, *ApJ*, **818**, 184
- Park, K., Wise, J. H., & Bogdanović, T. 2017, *ApJ*, **847**, 70
- Park, K., Wise, J. H., Bogdanović, T., & Ricotti, M. 2020, *ApJ*, **905**, 92
- Pensabene, A., Carniani, S., Perna, M., et al. 2020, *A&A*, **637**, A84
- Prieto, J., & Escala, A. 2016, *MNRAS*, **460**, 4018
- Regan, J. A., Johansson, P. H., & Haehnelt, M. G. 2014, *MNRAS*, **439**, 1160
- Regan, J. A., Wise, J. H., Woods, T. E., et al. 2020, *OJAp*, **3**, 15
- Rieke, M., Arribas, S., Bunker, A., et al. 2019, *BAAS*, **51**, 45
- Sakurai, Y., Inayoshi, K., & Haiman, Z. 2016, *MNRAS*, **461**, 4496
- Sakurai, Y., Yoshida, N., Fujii, M. S., & Hirano, S. 2017, *MNRAS*, **472**, 1677
- Salvaterra, R., Haardt, F., Volonteri, M., & Moretti, A. 2012, *A&A*, **545**, L6
- Sassano, F., Schneider, R., Valiante, R., et al. 2021, *MNRAS*, **506**, 613
- Sazonov, S. Y., Ostriker, J. P., & Sunyaev, R. A. 2004, *MNRAS*, **347**, 144
- Sądowski, A., Narayan, R., Tchekhovskoy, A., et al. 2015, *MNRAS*, **447**, 49
- Schaerer, D. 2003, *A&A*, **397**, 527
- Schramm, M., & Silverman, J. D. 2013, *ApJ*, **767**, 13
- Shakura, N. I., & Sunyaev, R. A. 1973, *A&A*, **24**, 337
- Shang, C., Bryan, G. L., & Haiman, Z. 2010, *MNRAS*, **402**, 1249
- Shankar, F., Weinberg, D. H., & Miralda-Escudé, J. 2009, *ApJ*, **690**, 20
- Shapiro, P. R., Iliev, I. T., & Raga, A. C. 1999, *MNRAS*, **307**, 203
- Shen, S., Mo, H. J., White, S. D. M., et al. 2003, *MNRAS*, **343**, 978
- Shull, J. M., & van Steenberg, M. E. 1985, *ApJ*, **298**, 268
- Sijacki, D., Springel, V., & Haehnelt, M. G. 2009, *MNRAS*, **400**, 100
- Smith, A., Becerra, F., Bromm, V., & Hernquist, L. 2017, *MNRAS*, **472**, 205
- Stewart, G. R., & Ida, S. 2000, *Icar*, **143**, 28
- Stone, J. M., & Pringle, J. E. 2001, *MNRAS*, **322**, 461
- Stone, J. M., Pringle, J. E., & Begelman, M. C. 1999, *MNRAS*, **310**, 1002
- Sugimura, K., Hosokawa, T., Yajima, H., Inayoshi, K., & Omukai, K. 2018, *MNRAS*, **478**, 3961
- Sugimura, K., Hosokawa, T., Yajima, H., & Omukai, K. 2017, *MNRAS*, **469**, 62



- Tagawa, H., Haiman, Z., & Kocsis, B. 2020, [ApJ](#), **892**, 36
- Takahashi, S. Z., Inutsuka, S.-i., & Machida, M. N. 2013, [ApJ](#), **770**, 71
- Takasao, S., Tomida, K., Iwasaki, K., & Suzuki, T. K. 2018, [ApJ](#), **857**, 4
- Takeo, E., Inayoshi, K., & Mineshige, S. 2020, [MNRAS](#), **497**, 302
- Takeo, E., Inayoshi, K., Ohsuga, K., Takahashi, H. R., & Mineshige, S. 2018, [MNRAS](#), **476**, 673
- Toomre, A. 1964, [ApJ](#), **139**, 1217
- Toyouchi, D., Hosokawa, T., Sugimura, K., Nakatani, R., & Kuiper, R. 2019, [MNRAS](#), **483**, 2031
- Toyouchi, D., Inayoshi, K., Hosokawa, T., & Kuiper, R. 2021, [ApJ](#), **907**, 74
- Valentini, M., Gallerani, S., & Ferrara, A. 2021, [MNRAS](#), **507**, 1
- Valiante, R., Schneider, R., Zappacosta, L., et al. 2018, [MNRAS](#), **476**, 407
- Venemans, B. P., Walter, F., Decarli, R., et al. 2017, [ApJ](#), **837**, 146
- Verner, D. A., Ferland, G. J., Korista, K. T., & Yakovlev, D. G. 1996, [ApJ](#), **465**, 487
- Visbal, E., Haiman, Z., & Bryan, G. L. 2015, [MNRAS](#), **453**, 4456
- Volonteri, M. 2012, [Sci](#), **337**, 544
- Volonteri, M., & Rees, M. J. 2005, [ApJ](#), **633**, 624
- Wang, F., Yang, J., Fan, X., et al. 2021, [ApJL](#), **907**, L1
- Wang, R., Carilli, C. L., Neri, R., et al. 2010, [ApJ](#), **714**, 699
- Wang, R., Wagg, J., Carilli, C. L., et al. 2013, [ApJ](#), **773**, 44
- Watarai, K.-y., Fukue, J., Takeuchi, M., & Mineshige, S. 2000, [PASJ](#), **52**, 133
- Wechsler, R. H., Bullock, J. S., Primack, J. R., Kravtsov, A. V., & Dekel, A. 2002, [ApJ](#), **568**, 52
- Whalen, D., & Norman, M. L. 2006, [ApJS](#), **162**, 281
- Willott, C. J., Delorme, P., Reyl  , C., et al. 2010, [AJ](#), **139**, 906
- Wise, J. H., Regan, J. A., O’Shea, B. W., et al. 2019, [Natur](#), **566**, 85
- Wise, J. H., Turk, M. J., & Abel, T. 2008, [ApJ](#), **682**, 745
- Wu, X.-B., Wang, F., Fan, X., et al. 2015, [Natur](#), **518**, 512
- Yajima, H., Ricotti, M., Park, K., & Sugimura, K. 2017, [ApJ](#), **846**, 3
- Yan, M., Sadeghpour, H. R., & Dalgarno, A. 1998, [ApJ](#), **496**, 1044
- Yang, J., Wang, F., Fan, X., et al. 2021, [ApJ](#), **923**, 262
- Yoshida, N., Omukai, K., & Hernquist, L. 2008, [Sci](#), **321**, 669
- Zhu, Q., Li, Y., Li, Y., et al. 2020, [arXiv:2012.01458](#)
- Zhu, Z., Hartmann, L., Gammie, C., & McKinney, J. C. 2009, [ApJ](#), **701**, 620
- Zhu, Z., & Stone, J. M. 2018, [ApJ](#), **857**, 34